

Uncovering spatio-temporal patterns in semiconductor superlattices by efficient data processing tools

F. Terragni and L. L. Bonilla

G. Millán Institute for Fluid Dynamics,

Nanoscience and Industrial Mathematics, and Department of Mathematics,

Universidad Carlos III de Madrid, 28911 Leganés, Spain

J. M. Vega*

E.T.S.I. Aeronáutica y del Espacio,

Universidad Politécnica de Madrid,

28040 Madrid, Spain

**Corresponding author: josemanuel.vega@upm.es*

(Dated: October 1, 2021)

Abstract

Time periodic patterns in a semiconductor superlattice, relevant to microwave generation, are obtained upon numerical integration of a known set of drift-diffusion equations. The associated spatio-temporal transport mechanisms are uncovered by applying (to the computed data) two recent data processing tools, known as the higher order dynamic mode decomposition and the spatio-temporal Koopman decomposition. Outcomes include a clear identification of the asymptotic self-sustained oscillations of the current density (isolated from the transient dynamics) and an accurate description of the electric field traveling pulse in terms of its dispersion diagram. In addition, a preliminary version of a novel data-driven reduced order model is constructed, which allows for extremely fast online simulations of the system response over a range of different configurations.

I. INTRODUCTION

Semiconductor superlattices are periodically layered structures, which are formed by epitaxial growth of layers of two or more different semiconductors with similar lattice parameters. These superlattices show damped, high-frequency, spatially uniform Bloch oscillations [1, 2]. In principle, it should be possible to find inhomogeneous Bloch oscillations that coexist with much slower self-sustained oscillations due to periodic generation and motion of charge dipoles [3]. In experiments, the frequency range of the more robust self-sustained oscillations in semiconductor superlattices may be as large as 100–200 GHz, which makes them useful in, e.g., fast oscillators and detectors [4], whereas similar self-sustained oscillations in quantum cascade laser devices may reach ultra-high frequencies well in the THz range [5], which are needed in, e.g., nano-patterned antennas [6]. Superlattice-based devices exhibit very different spatio-temporal patterns and rich nonlinear dynamics, including static high-field domains, excitability due to collective charge dynamics, as well as self-sustained periodic, quasi-periodic, and chaotic current oscillations [4, 7–10]. Under an external magnetic field, which is tilted with respect to the growth direction, electron motion in the superlattice miniband is two-dimensional (2D). Experiments show a variety of high-frequency periodic and chaotic oscillations of the current [11, 12]. It is interesting that single electron motion in a miniband exhibits Hamiltonian chaos and stochastic webs [11–13], whereas collective charge motion, taking scattering into account through the Boltzmann-Bhatnagar-Gross-Krook (BBGK) equation, displays dissipative chaos through 2D patterns [14].

In this work, we consider n -doped, strongly coupled one miniband semiconductor superlattices [4, 7, 15–17]. Under appropriate dc voltage bias and configuration parameters, these superlattices exhibit self-sustained oscillations of the current, which have been the subject of extensive theoretical and experimental studies [4]. The relevant state variables in a dc voltage-biased superlattice configuration are the time-dependent scalar *current density* and the distributed *electric field*. Control parameters such as the width of the layers, the doping density, the voltage bias, and the conductivity at the injecting contact (cathode) determine the existence, shape, and frequency of the oscillations of the current density through the superlattice [4, 7]. The evolution of the state variables can be computed using one of the numerical methods presented in [18], which simulate the electron transport in a single miniband superlattice by integrating either the governing BBGK kinetic equations or a drift-diffusion

approximation of the latter. In the spatially one-dimensional (1D) case, numerical simulations show that, for convenient values of the various involved nondimensional parameters, the electric field exhibits an interesting spatio-temporal pattern. After a transient, the dynamics become temporally periodic, showing a *traveling solitary wave* for the electric field in the bulk (which can also be seen as a charge dipole wave). This wave goes from the cathode to the anode (as in the Gunn effect of bulk semiconductors [7, 19–23]) and, when it reaches the anode, another wave is created at the cathode, in such a way that the process is periodically repeated. Correspondingly, the current through the superlattice displays self-sustained oscillations. The current self-oscillations and the spatio-temporal patterns of the electric field and charge density are highly non-monochromatic, namely they show a *large number of harmonics*. The intrinsic spectral properties and the amplitude of these phenomena depend on the specific superlattice configuration and are important to fully characterize the underlying electron transport. Thus, extracting the frequency spectrum with accuracy, analyzing its variation in terms of the main involved parameters, and describing the evolution of the state variables through the structure can provide interesting insights into these devices and their setup.

In this paper, numerically computed data for the current density and the electric field during current self-oscillations will be treated using two recently introduced *data processing tools*: the *higher order dynamic mode decomposition* (HODMD) [24] and the *spatio-temporal Koopman decomposition* (STKD) [25]. These decompositions isolate the dynamical features behind the given data, quantitatively uncovering the dominant components of complex nonlinear signals. For the superlattice self-oscillations, we use data extracted from the transient dynamics that decay to the periodic attractor to isolate and characterize the latter. Specifically, the HODMD and STKD methods extract the frequencies and the growth rates of spatio-temporal patterns. Applications to other systems can be found in [26].

The HODMD method deals with spatio-temporal data associated with dynamics exhibiting time-dependent exponential growth or decay and oscillations. Firstly, we define a time-dependent vector state variable \mathbf{q} comprising the total current density and the electric field at a number of grid points. Then, we compute snapshots of \mathbf{q} at temporally equispaced values of t in a limited timespan. The HODMD outcome is a discrete Fourier-like expansion

of the form

$$\mathbf{q}_k \equiv \mathbf{q}(t_k) \simeq \sum_{n=1}^N a_n \mathbf{u}_n e^{(\delta_n + i\omega_n)t_k}, \quad (1)$$

with $t_k = (k-1)\Delta t$, for $k = 1, \dots, K$. Here, $a_n > 0$ are real *amplitudes*, \mathbf{u}_n are conveniently normalized (generally complex) *modes*, and δ_n and ω_n are the associated *growth rates* and *frequencies*, respectively. It is important to note that replacing t_k by t in eq.(1) (which involves automatic time interpolation) leads to the continuous expansion

$$\mathbf{q}(t) \simeq \sum_{n=1}^N a_n \mathbf{u}_n e^{(\delta_n + i\omega_n)t}, \quad (2)$$

which gives an analytical representation of the underlying dynamics. When all growth rates, δ_n , are zero (or conveniently small in absolute value), then the resulting modes **are called permanent modes and the associated** dynamics correspond to an *attractor*. If all frequencies ω_n are commensurable, then the attractor is *periodic*, while it is quasi-periodic if some of the involved frequencies are incommensurable (within a small threshold). It is worth mentioning that, for chaotic attractors, an infinite number of modes would be involved and the analysis by means of HODMD would be subtle [24]. If, in addition to the permanent modes, there is a second group of modes that exhibit clearly negative growth rates, then the expansion (2) corresponds to a *transient behavior approaching an attractor*. The latter can be identified by retaining in the expansion only those (permanent) modes with $\delta_n = 0$ (or suitably small). Such calculation of the final attractor via HODMD extrapolation accelerates the computation of asymptotic dynamics [27]. Collecting only the decaying modes (with non-small negative δ_n) gives the strictly decaying approach to the attractor. On the contrary, if some growth rates are strictly positive and the remaining ones are small in absolute value or equal to zero, then the expansion (2) yields an unstable behavior departing from (unstable) permanent dynamics, which is useful to identify *instabilities* [28]. However, this latter scenario will not arise in the analysis carried out in the present paper.

Besides uncovering spatio-temporal patterns, the expansion (2) can be used to build a purely data-driven *reduced order model* (ROM), able to simulate *online* the operation of the underlying dynamical system. This ROM is extremely fast because it only requires performing algebraic computations, being thus appropriate for *optimization* [29] and *real-time active control* [30]. The superlattice ROM will be used to reconstruct the spatio-temporal pattern of current self-oscillations for a range of values of the injecting contact

conductivity. Importantly, the ROM uses numerical data for very few conductivity values, while efficiently predicting the superlattice response for many different conductivity values. Furthermore, the same approach may be extended to predictions of the device response in multi-parameter searches.

The STKD method works for dynamics exhibiting exponential/oscillatory behavior in both the temporal variable and one or more distinguished spatial variables (called *longitudinal* variables). Focusing on the simplest *spatially 1D* case with one scalar state variable, the STKD method leads to the continuous expansion

$$q(x, t) \simeq \sum_{m=1}^M \sum_{n=1}^N a_{mn} u_{mn} e^{(\nu_m - i\kappa_m)x + (\delta_n + i\omega_n)t}. \quad (3)$$

Here, ν_m and δ_n are *spatial* and *temporal* growth rates, respectively, while κ_m and ω_n are *wavenumbers* and *frequencies*, respectively. The real *amplitudes* $a_{mn} > 0$ and the generally complex *modes* u_{mn} (with $|u_{mn}| = 1$) depend on the two indices, m and n . Note that, if $\omega_n/\kappa_m = c$, then the whole pattern is a *pure traveling wave*, with *phase velocity* c . In this case, the *dispersion diagram* of ω_n vs. κ_m becomes a straight line passing through the origin. When the dispersion diagram consists of a family of parallel, oblique straight lines, the pattern is a *modulated traveling wave*. For superlattice self-oscillations, the STKD method produces an accurate reconstruction of the spatio-temporal pattern of the periodic attractor, but it involves too many spatial and temporal modes. Thus, it is computationally too costly to yield a fast ROM.

The computational costs of the various methods and codes can be measured, and compared among each other, in terms of the required CPU times. These will be given below for representative cases, taking into account that all computations were performed using standard (uncompiled) MATLAB in a desktop PC, with a microprocessor Intel Core i7-6500U at 2.5GHz.

The remainder of this paper is structured as follows. The drift-diffusion model equations and the numerical solver for the considered semiconductor superlattice are described in Section II. The main results, in connection with uncovering spatio-temporal patterns using the HODMD method for a representative superlattice configuration, are given in Section III. Section IV shows how the STKD method characterizes the evolution of the electric field. Section V contains a preliminary version of a novel HODMD-based data-driven ROM for the present system, while the main conclusions of the paper are found in Section VI. Appendices

A and B provide concise descriptions of the HODMD and STKD methods, respectively.

II. MODEL EQUATIONS AND NUMERICAL SOLVER

In nondimensional form, the BBGK-Poisson kinetic equations for the distribution function, $f(x, k, t)$, of a one miniband semiconductor superlattice are [18]

$$\lambda \left(\frac{\partial f}{\partial t} + \gamma \sin(k) \frac{\partial f}{\partial x} \right) + F \frac{\partial f}{\partial k} = \frac{f^{FD} - f}{\tau_e} - \frac{\tau_e^2 - 1}{2\tau_e} [f - f(x, -k, t)], \quad (4a)$$

$$\frac{\partial F}{\partial x} = n - 1, \quad (4b)$$

$$n = \frac{1}{2\pi} \int_{-\pi}^{\pi} f(x, k, t) dk = \frac{1}{2\pi} \int_{-\pi}^{\pi} f^{FD}(k; \mu(n)) dk, \quad (4c)$$

$$f^{FD}(k; \mu) = \alpha \ln [1 + \exp(\mu - \mathcal{E}(k))]. \quad (4d)$$

Here, $n(x, t)$ and $F(x, t)$ are the electron density and the electric field inside the superlattice, respectively. The superlattice has a single populated miniband with a tight-binding dispersion relation $\mathcal{E}(k) = \beta(1 - \cos k)$ between the energy and the wavevector k . $f^{FD}(k; \mu)$ is the local Fermi-Dirac equilibrium distribution function and μ is the chemical potential, which is a function of the electron density given by the solution of eq.(4c). In addition, λ , γ , τ_e , α , and β are dimensionless parameters, where λ is the ratio of the mean time between collisions to the characteristic electron transport time, which is small for most superlattices. In [17], this fact was exploited by using the Chapman-Enskog perturbation method (in the limit as $\lambda \rightarrow 0$) to derive a *drift-diffusion* equation for $F(x, t)$ which, in nondimensional form, is [18]

$$\frac{\partial F}{\partial t} + \mathcal{A} \frac{\partial F}{\partial x} + \mathcal{B} \frac{\partial^2 F}{\partial x^2} + \mathcal{C} J = \mathcal{D}, \quad (5)$$

for $0 < x < L$. Here, $J(t)$ is the (scalar) total current density and L is the nondimensional length of the superlattice. The coefficients \mathcal{A} , \mathcal{B} , \mathcal{C} , and \mathcal{D} appearing in this equation depend on F , its first and second spatial derivatives, and the superlattice physical properties. Their specific form can be found in [17, 18] but it will not be needed for our data-driven analysis. Equation (5) is solved with a nondimensional Ohmic boundary condition at the injecting contact (cathode) and a zero-charge boundary condition at the receiving contact (anode) [17], namely

$$\frac{\partial F(0, t)}{\partial t} + \sigma F(0, t) = J(t), \quad \frac{\partial F(L, t)}{\partial x} = 0, \quad (6)$$

where $\sigma > 0$ is the *contact conductivity*. Finally, the total current density is determined by imposing the *dc* voltage bias condition,

$$V_{\text{bias}} = \int_0^L F(x, t) dx, \quad (7)$$

where V_{bias} is a given positive constant.

As explained in [17], numerical solutions of the model equations (5)-(7) provide accurate values of the oscillation frequencies and their dependence on the different parameters as observed in experiments [16, 31]. Experimental observations in strongly coupled one miniband semiconductor superlattices resolve oscillation frequencies and Fourier spectra, but they do not provide *time resolved* currents as functions of time because the involved frequencies are too high (GHz-THz range) [4, 11, 12, 16, 31]. Thus, we cannot directly compare numerically obtained time-dependent current densities or electron densities with experiments. This also precludes comparison of experiments and predictions of driven chaos (by dc and ac voltage) obtained by numerically simulating eqs. (5)-(7) or related models [32]. In any event, for the model equations and the set of parameter values considered in the present work, with constant V_{bias} , the asymptotic dynamics are always periodic. More complex oscillations (either quasi-periodic or chaotic) may be reproduced by setting a voltage varying in time. On the other hand, weakly coupled superlattices are described by mathematical models different from the equations we study in this paper. They present oscillations in the MHz range and permit detailed comparison of theory with time resolved current from experiments [4], which includes spontaneous [8, 9, 33] and driven [34–36] chaos.

The numerical integration of eqs.(5)–(7) is carried out by means of a solver described in [18] (see also [37] for an analysis of the numerical method). Specifically, spatial discretization is performed via centered finite differences for the spatial derivatives and the composite Simpson’s rule to evaluate the right-hand side of eq.(7), while temporal integration is performed using an improved implicit Euler method.

The *numerical solver* outlined above, whose convergence order is approximately quadratic in space and linear in time, will be used throughout the paper to both calculate the snapshots needed by the data processing methods and compute the reference, ‘exact’ solutions to compare with the generated approximations. Concerning the computational cost, considering the time interval $0 \leq t \leq 300$ (which will be repeatedly used in this work) and the standard desktop PC indicated at the end of Section I, each run requires ~ 20 CPU minutes.

III. SPATIO-TEMPORAL PATTERNS IN A SEMICONDUCTOR SUPERLATTICE

In this section, we first present some representative results obtained via direct numerical simulation. Then, the HODMD method is applied to compute, isolate, and describe the periodic attractor and the transient dynamics decaying to the attractor for both the current density and the electric field. Finally, it is shown that HODMD improves/outperforms a fast Fourier transform (FFT) calculation of the asymptotic dynamics.

Here, we consider the model equations described in Section II, eqs.(5)–(7), with the following representative parameter values

$$L = 33.19, \quad \sigma = 0.37, \quad V_{\text{bias}} = 1.2 L. \quad (8)$$

The initial conditions will always be taken as

$$F(x, 0) = 1.2, \quad J(0) = 1.2 \sigma. \quad (9)$$

In order to obtain the needed data, the numerical solver mentioned in Section II is run using

$$I = 481 \quad (10)$$

equispaced grid points in the spatial domain and a time step equal to 0.01 in the time interval

$$0 \leq t \leq 300. \quad (11)$$

With this selection of the discretization parameters, the expected relative *root mean square* (RMS) accuracy of the numerical simulations is $\sim 10^{-3}$.

A. The numerically computed pattern

Figure 1 shows how the current density in the time interval (11) becomes time periodic after a transient. The transient duration, which depends on how far from the attractor the initial condition is, cannot be appreciated in the plot. However, the highly non-monochromatic character of the attractor is clearly visible. For the same time interval, Fig.2 displays the spatio-temporal density plot of the electric field $F(x, t)$. As anticipated, the diagram shows a solitary wave that is created at $x = 0$ (cathode) and propagates towards $x = L$ (anode).

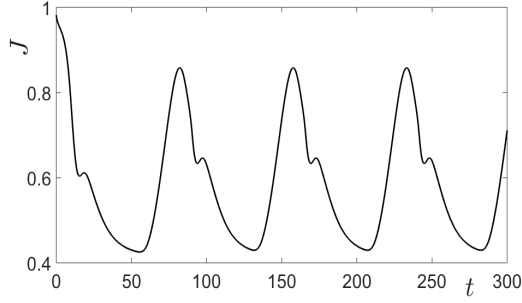


FIG. 1. Temporal evolution of the current density in the considered timespan.

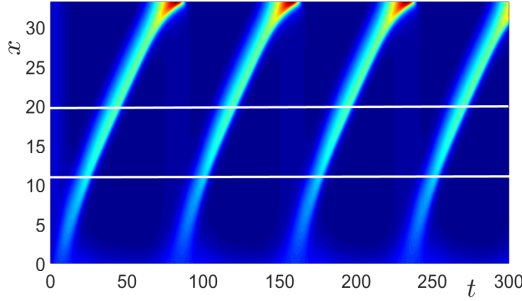


FIG. 2. Spatio-temporal color diagram for the evolution of the electric field in the considered timespan. The intensity of F varies from blue to red as F increases. The two horizontal white lines indicate the values $x = \tilde{x}_1$ and $x = \tilde{x}_2$, as defined in eq.(12)

As the solitary wave travels, its propagation velocity decreases, while the electric field peak increases. Although not clearly appreciated in the figure, the background electric field must decrease along the wave journey. This is because the voltage bias, defined in eq.(7), remains constant as time proceeds, while the area behind the solitary wave increases. On the other hand, this condition is consistent with the fact that, as seen in Fig.2, each time a solitary wave reaches the boundary $x = L$, another wave is created at $x = 0$.

However, illustrative as it is, the spatio-temporal diagram in Fig.2 does not have sufficient contrast to quantitatively compare different approximations. A more quantitative (though less complete in the spatial coordinate) account of the electric field is given in Fig.3, which shows the evolution of F at two representative points inside the spatial domain, namely

$$x = \tilde{x}_1 = \frac{L}{3} \quad \text{and} \quad x = \tilde{x}_2 = \frac{3L}{5}. \quad (12)$$

These points are the horizontal white lines in Fig.2. We shall use plots similar to Fig.3 to compare the electric field computed by direct numerical simulations with its various approximations obtained via the HODMD method.

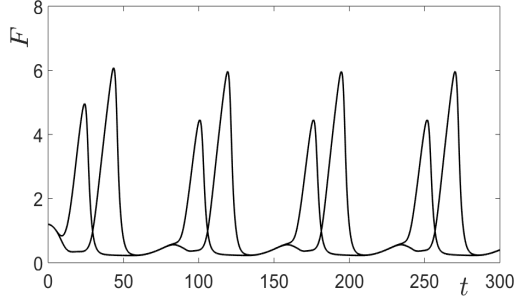


FIG. 3. Plots of $F(\tilde{x}_1, t)$ and $F(\tilde{x}_2, t)$ vs. t , with \tilde{x}_1 and \tilde{x}_2 as defined in eq.(12). Since $\tilde{x}_1 < \tilde{x}_2$, the two curves can be distinguished because, consistently with Fig.2, $F(\tilde{x}_2, t)$ shows higher peaks than $F(\tilde{x}_1, t)$.

B. Uncovering spatio-temporal patterns via HODMD

We now apply several variants of the HODMD method to the superlattice dynamics discussed in the last subsection. To this end, we consider $K = 3000$ temporally equispaced snapshots at

$$t_k = (k - 1) \Delta t, \quad \text{for } k = 1 \dots, K. \quad (13)$$

Each snapshot contains the values of both the scalar current density J and the electric field F at the $I = 481$ spatial grid points used in the numerical simulations. In other words, for $k = 1, \dots, K$, the snapshot \mathbf{q}_k is the $(I + 1)$ -vector given by

$$\mathbf{q}_k = [J(t_k), F(x_1, t_k), F(x_2, t_k), \dots, F(x_I, t_k)]^\top. \quad (14)$$

Applying HODMD to these snapshots, we obtain the counterpart of the discrete expansion in eq.(1). Replacing t_k by t in this expansion leads to its continuous counterpart, given by eq.(2), which invoking the structure of the snapshots (14) yields the evolution of both $J(t)$ and $F(x_i, t)$. As a result, the current density and the electric field are approximated as

$$J(t) \simeq \sum_{n=1}^N a_n u_n^J e^{(\delta_n + i\omega_n)t}, \quad (15)$$

$$F(x_i, t) \simeq \sum_{n=1}^N a_n u_n^F(x_i) e^{(\delta_n + i\omega_n)t}, \quad (16)$$

for $i = 1, \dots, I$. Here, the amplitudes a_n are common to both expansions, as are the growth rates δ_n and the frequencies ω_n . In fact, for the periodic attractors computed below, the involved frequencies will include the zero frequency, which is associated with the *temporal*

mean field, while the remaining ones will be *positive* and *negative harmonics* of a *fundamental frequency* ω_1 . Namely, they will be of the form

$$\omega_p = p\omega_1, \text{ for } p = -P, -(P-1), \dots, 0, \dots, P-1, P. \quad (17)$$

This permits rewriting the expansions (15)-(16) as

$$J(t) \simeq \sum_{p=-P}^P a_p u_p^J e^{ip\omega_1 t}, \quad (18)$$

$$F(x_i, t) \simeq \sum_{p=-P}^P a_p u_p^F(x_i) e^{ip\omega_1 t}, \quad (19)$$

where the growth rates have been set to zero because we are considering attractors.

In the following, we will apply the HODMD method to first identify both the final periodic attractor and the strict decay to the attractor in the transient stage. Then, the attractor will be computed by performing various applications of *extrapolated* HODMD, using data extracted in timespans of limited temporal length. In these cases, with the standard PC described at the end of Section I, the required CPU time to compute the expansions (18)-(19) is ~ 1 CPU minute.

Identifying the attractor and the transient decaying dynamics using snapshots in the whole timespan

To begin with, the HODMD method is applied to the entire set of $K = 3000$ snapshots, defined in eq.(14). After a slight calibration, the tunable parameters of the HODMD method (see Appendix A), namely the dimension reduction threshold, ε_{SVD} , the mode truncation threshold, ε_{DMD} , and the index d to apply the DMD- d algorithm, are selected as

$$\varepsilon_{\text{SVD}} = 10^{-7}, \quad \varepsilon_{\text{DMD}} = 10^{-4}, \quad \text{and} \quad d = 25. \quad (20)$$

Using these values, the DMD-25 algorithm reconstructs the given snapshots, retaining $N = 113$ modes. To elucidate the performance of the HODMD method, we define the *relative root mean square* (RRMS) error

$$\text{RRMS error} = \sqrt{\frac{\sum_{k=1}^K \|\mathbf{q}_k^{\text{approx}} - \mathbf{q}_k\|_2^2}{\sum_{k=1}^K \|\mathbf{q}_k\|_2^2}}, \quad (21)$$

where $\|\cdot\|_2$ denotes the usual Euclidean norm. For the current density and the electric field, the RRMS errors are $\sim 9.4 \cdot 10^{-4}$ and $2.4 \cdot 10^{-3}$, respectively. The approximations of both state variables are illustrated in Fig.4. It is interesting to point out that using the DMD-1

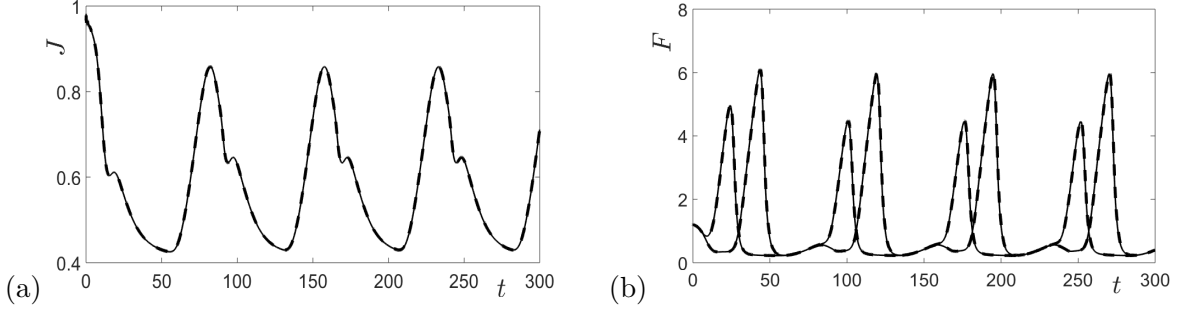


FIG. 4. Counterparts of Figs.1 (a) and 3 (b) for the HODMD method application with tunable parameters as in eq.(20) and $K = 3000$ snapshots in $0 \leq t \leq 300$. The original data are plotted with thin solid lines, while the reconstructed data with thick dashed lines.

algorithm (namely, standard DMD [38, 39]), with the same values of thresholds ε_{SVD} and ε_{DMD} given in eq.(20), the RRMS errors for J and F are much larger, namely ~ 0.034 and 0.15 , respectively. The worse performance of the DMD-1 algorithm is due to the fact that, to the approximation relevant here, the spatial complexity (i.e., the rank of the set of modes), 64, is clearly smaller than the spectral complexity (i.e., the number N), 113. The number of modes retained by the DMD-1 algorithm is 110, namely it is slightly smaller than the spectral complexity (see Appendix A for further details on this issue).

Inspection of the diagrams of the growth rates and amplitudes vs. the frequencies is enlightening. As can be seen in Fig.5, both plots are symmetric around $\omega = 0$, which is due to the fact that the considered data are real. And, what is more important in the present context, plot (a) shows two distinguishable groups of growth rates, which are separated by a wide gap between $\delta \sim -10^{-4}$ and $\delta \sim -10^{-2}$. These two groups give rise to different spatio-temporal patterns, which can be identified as anticipated in Section I.

- Since the 47 points in the lower group in Fig.5–(a) exhibit very small growth rates in absolute value (namely, smaller than $\sim 10^{-4}$), this group is seemingly associated with the periodic *final attractor*. These (small but) non-zero growth rates are either positive or negative, but this is an artifact due to numerical errors, both in the given data and in the HODMD computations. In fact, they are set to zero in the attractor reconstruction.

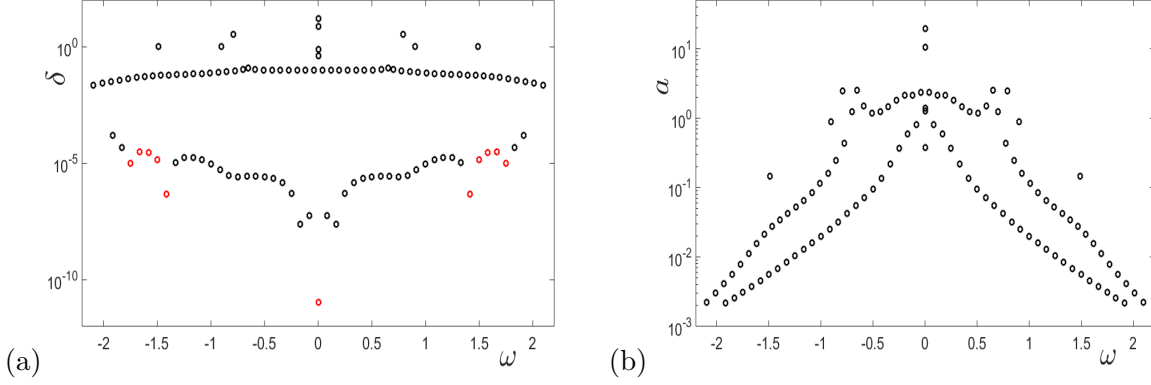


FIG. 5. Growth rates (a) and amplitudes (b) vs. the frequencies for the retained modes, using the HODMD method with tunable parameters as in eq.(20) and $K = 3000$ snapshots in $0 \leq t \leq 300$. In plot (a), positive and negative growth rates are displayed in red and black, respectively.

- The upper group of points in Fig.5–(a) exhibits significant, negative growth rates. Thus, it seems to be associated with the strictly *decaying approach to the attractor*.

These two groups are now analyzed to uncover the associated spatio-temporal patterns.

For the 47 points in the lower group, the counterpart of Fig.5 is given in Fig.6. Note that

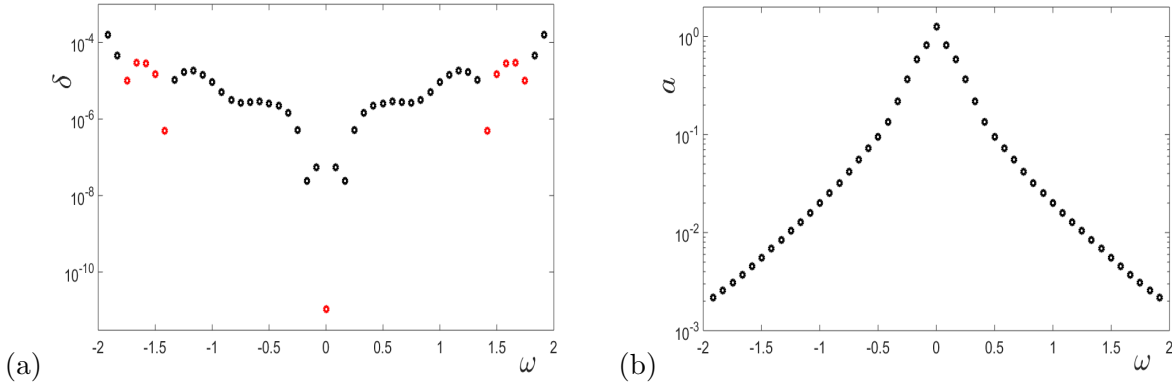


FIG. 6. Counterpart of Fig.5, considering only the lower group of points in both plots.

the plot of the amplitudes vs. the frequencies shows spectral decay, which is always seen in data resulting from smooth periodic dynamics [24]. Moreover, in addition to the frequency $\omega = 0$ (which corresponds to the temporal mean field), the remaining 23 positive and 23 negative frequencies are positive and negative harmonics of the *fundamental frequency*

$$\omega_1 = 8.3212 \cdot 10^{-2}. \quad (22)$$

Namely, the various frequencies are of the form $\pm p \omega_1$ for $p = 0, 1, \dots, 23$, with four exact significant digits. In fact, the fundamental frequency ω_1 is calculated as follows. First, the

47 frequencies are sorted in increasing order. Then, the differences between two consecutive frequencies are calculated and seen to be approximately constant along the sequence. Finally, ω_1 is computed as the arithmetic mean of these differences.

The value of ω_1 in eq.(22) gives the period of the orbit as

$$T_1 = 2\pi/\omega_1 = 75.508. \quad (23)$$

On the other hand, as anticipated in Section I, retaining only the 47 amplitudes, modes, and frequencies appearing in Fig.6, and setting to zero the associated growth rates, the expansions (18)-(19) give the evolution of the current density and the electric field for the periodic attractor. It is interesting to note that, in the resulting expansions, the spatial complexity is 46, while the spectral complexity is 47. These expansions give (an approximation of) the periodic attractor in any timespan. Then, the attractor is computed in the whole time interval $0 \leq t \leq 300$ (although it approximates the actual dynamics only after the transient stage). In fact, this computation of the asymptotic spatio-temporal pattern will be compared with other approximations obtained below. For illustration of the periodic attractor, the current density and the electric field at $x = \tilde{x}_1$ and $x = \tilde{x}_2$ (see eq.(12)) are given in Fig.7.

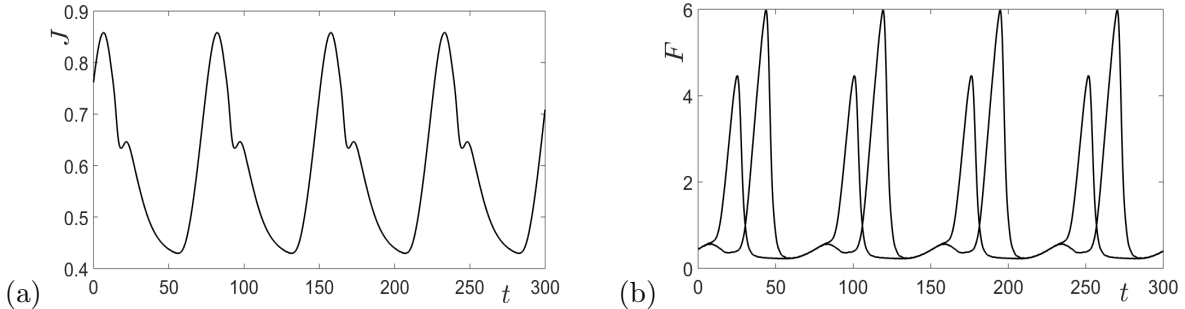


FIG. 7. Counterpart of Fig.4 for the periodic attractor.

The spatio-temporal pattern associated with the upper group of $113 - 47 = 66$ points in Fig.5 is now analyzed. In other words, the associated amplitudes, modes, growth rates, and frequencies are used in the expansions (15)-(16), which permits reconstructing the transient dynamics that obviously decay to zero as time goes to infinity. Also, the purely decaying pattern is a good quantitative description of the difference between the whole dynamics and the periodic attractor, which is seen in Fig.8. However, the temporal extent of the transient stage is not evident in this figure to the naked eye. A good means to appreciate

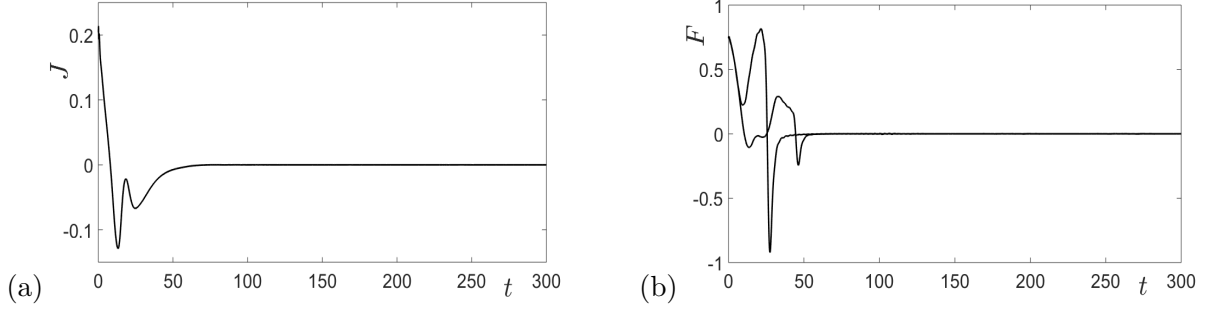


FIG. 8. Counterpart of Fig.7 for the purely decaying dynamics.

the temporal convergence of the transient to the attractor is to compute, for each value of t , the spatial RMS norm of the electric field for the strictly decaying dynamics. This RMS norm, denoted as E , is plotted vs. time in Fig.9, which shows that such norm decreases

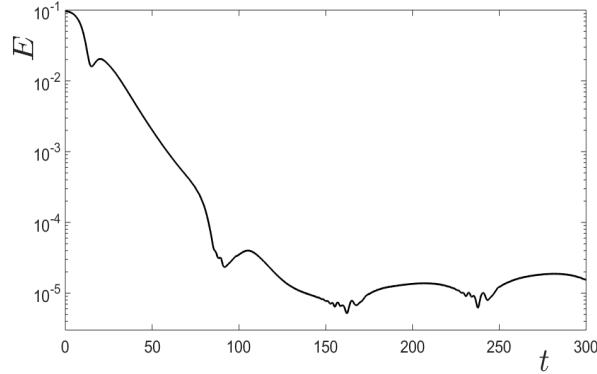


FIG. 9. Spatial RMS norm of the electric field for the strictly decaying dynamics.

(non-monotonously) until $t \sim 150$, where it saturates due to computational errors. After this value of t , it remains approximately constant, except for some oscillations. Thus, to the approximation relevant here, the transient stage can be assumed to be

$$0 \leq t < 150. \quad (24)$$

In this interval, the overall decrease of the strictly decaying dynamics, as seen in the semi-logarithmic plot in Fig.9, is roughly a straight line, whose negative slope is consistent with the overall damping rate for the upper group of points in Fig.5-(a), which is $-\delta \sim 2 \cdot 10^{-2}$.

Computing the attractor via HODMD extrapolation

Now, let us consider the approach outlined in Section I to approximate the periodic attractor by HODMD *extrapolation* from the temporal interval (24), namely using $K = 1500$ snapshots in the transient stage. After some slight calibration (controlling the RRMS error, as defined in eq.(21), of the HODMD reconstruction in the transient stage), the HODMD tunable parameters are selected as

$$\varepsilon_{\text{SVD}} = 10^{-7}, \quad \varepsilon_{\text{DMD}} = 10^{-4}, \quad \text{and} \quad d = 45. \quad (25)$$

Using these values, the application of HODMD to the selected $K = 1500$ snapshots reconstructs the latter with a RRMS error $\sim 5.91 \cdot 10^{-3}$ and $\sim 6.95 \cdot 10^{-3}$ for the current density and the electric field, respectively, retaining $N = 88$ modes. The associated growth rates, amplitudes, and frequencies are displayed in Fig.10. As seen in plot (a), the retained growth

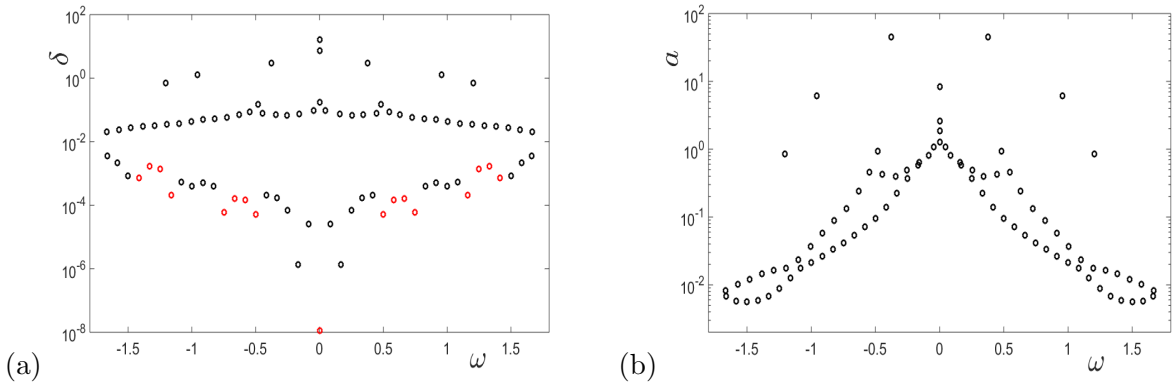


FIG. 10. Counterpart of Fig.5 for the application of HODMD to snapshots contained in the transient stage (24), with the tunable parameters given in eq.(25).

rates are organized in two groups, separated by a gap around $\delta = -10^{-2}$. As in the previous case, this yields two groups of modes. The upper group seemingly corresponds to the purely decaying dynamics and the lower group, which contains 41 points, to the periodic attractor. The approximation of the periodic attractor can be computed beyond the transient stage by extrapolation, using the amplitudes, modes, and frequencies associated with the lower group, and proceeding as anticipated in Section I. It turns out that:

- The obtained approximation of the fundamental frequency differs from the value in eq.(22) by a relative error $\sim 5.11 \cdot 10^{-4}$.

- The approximation of the periodic attractor in the timespan $150 \leq t \leq 300$ is quite similar to its counterpart in Fig.7. Indeed, the RRMS difference between them is $\sim 1.29 \cdot 10^{-3}$ for the current density and $\sim 9.11 \cdot 10^{-3}$ for the electric field. Thus, HODMD extrapolation yields an accurate reconstruction of the attractor only using numerical data in the transient stage, which, in the present case, divides by two the CPU time of computing the snapshots.

These results are illustrated in Fig.11, which shows a reasonably good approximation in

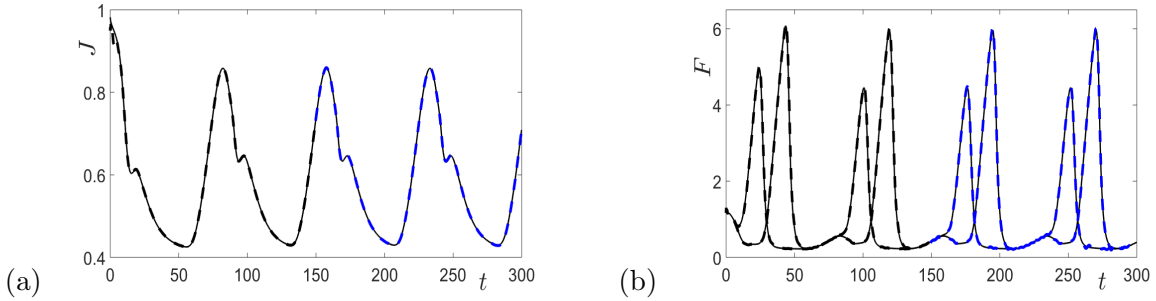


FIG. 11. Counterpart of Fig.4 when applying extrapolated HODMD using snapshots in the transient stage (24), with the tunable parameters in eq.(25). In both plots, the original data are shown with thin solid lines, the reconstructed data in the transient stage with thick dashed black lines, and the extrapolated data with thick dashed blue lines.

both the transient timespan and beyond.

As a second test case for HODMD temporal extrapolation, we reconstruct the attractor using snapshots contained in the last third of the considered timespan, namely in

$$200 \leq t \leq 300. \quad (26)$$

Note that this timespan is expected to be in the region where the dynamics are already very close to the periodic attractor. The HODMD method is applied with the following HODMD tunable parameter values

$$\varepsilon_{\text{SVD}} = 10^{-8}, \quad \varepsilon_{\text{DMD}} = 10^{-3}, \quad \text{and} \quad d = 20. \quad (27)$$

Results show reconstructions of the current density and the electric field, in the interval (26), within a RRMS error, as defined in eq.(21), $\sim 1.3 \cdot 10^{-4}$ and $\sim 1.5 \cdot 10^{-3}$, respectively, retaining $N = 51$ modes. The diagrams giving the retained growth rates and amplitudes

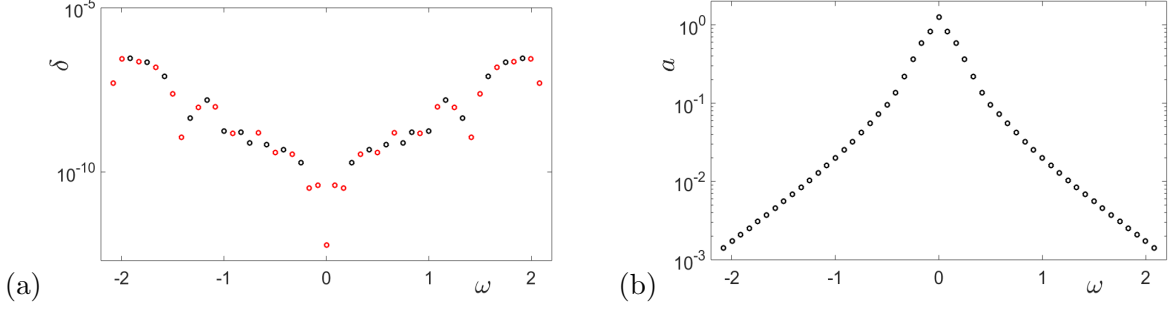


FIG. 12. Counterpart of Fig.10 for the application of HODMD to snapshots contained in the timespan (26), with the tunable parameters given in eq.(27).

vs. the frequencies are displayed in Fig.12. Note that all growth rates are very small in absolute value, namely smaller than $\sim 10^{-6}$, while the amplitudes exhibit spectral decay. The frequencies include the zero frequency (related to the temporal mean field) together with 25 positive and 25 negative harmonics of a fundamental frequency. The latter coincides with the value in eq.(22) within a relative error $\sim 1.5 \cdot 10^{-4}$. Also, the periodic attractor computed by HODMD backward extrapolation differs from its counterpart in Fig.7 by a RRMS error $\sim 1.5 \cdot 10^{-4}$ and $\sim 1.6 \cdot 10^{-3}$ for the current density and the electric field, respectively. These good results are illustrated in Fig.13. As can be seen in this figure, the backward

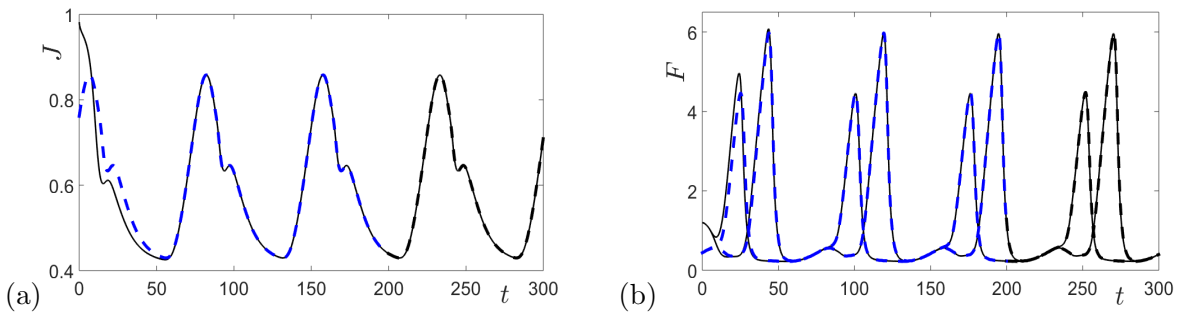


FIG. 13. Counterpart of Fig.11 when applying extrapolated HODMD using snapshots in the timespan (26), with the tunable parameters given in eq.(27).

extrapolation separates from the original data in the transient stage since, in the present case, it yields the periodic attractor by construction.

C. Comparison with results obtained by the FFT

In this subsection, the illustrated HODMD-based results are compared with those obtained using the MATLAB function ‘fft’, which implements a standard algorithm based on the discrete Fourier transform (DFT). Recall that FFT applies DFT to the given data, which means that the method somewhat assumes that the dynamics are periodic, with a period equal to the temporal interval where the data have been computed. This spurious period introduces *sideband artifacts*, consisting in erroneous frequencies that roughly concentrate (with small amplitudes) around the actual frequencies.

For illustration, only data regarding the current density will be used. First, the FFT is applied to the values of the current density computed by the numerical solver described in Section II at $K = 3000$ time instants, as in eq.(13), collected in the timespan (11), $0 \leq t \leq 300$, and sampled at distance $\Delta t = 0.1$. Thus, the sampling frequency is the same as the one implicit in the application of HODMD in the previous subsection. Plot (a) in Fig.14 shows the absolute value of the FFT-calculated amplitudes vs. the frequencies.

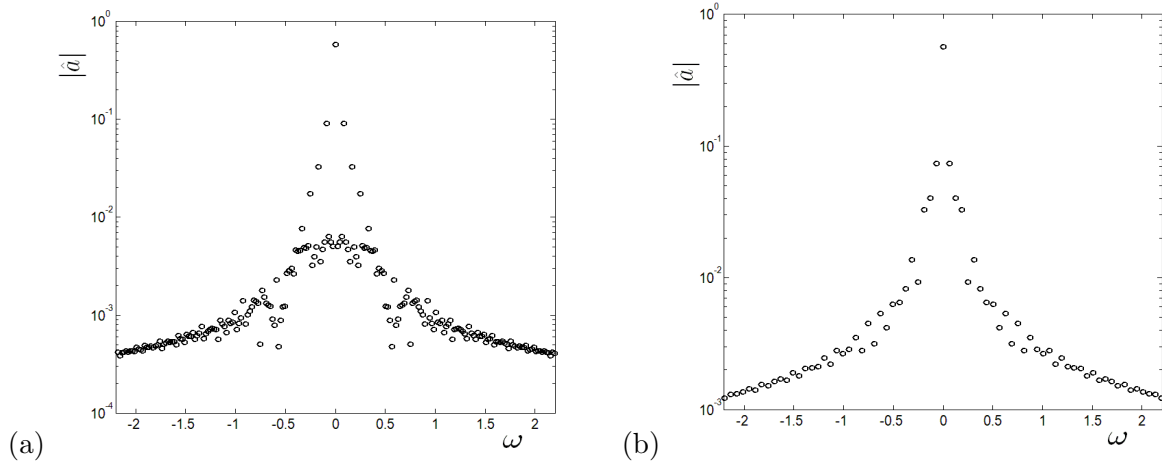


FIG. 14. Fourier amplitudes vs. the frequencies obtained via FFT applied to data of the current density in the temporal intervals $0 \leq t \leq 300$ (a) and $200 \leq t \leq 300$ (b).

As can be seen, the FFT captures a large number of frequencies, which include the mean field frequency $\omega = 0$, the fundamental frequency $\omega_1 = 8.378 \cdot 10^{-2}$, and three harmonics of it, all with reasonable accuracy. The remaining frequencies computed by the FFT are all spurious and include a few (positive and negative) subharmonics of the fundamental frequency. This is obviously much worse than the outcome of HODMD that, in addition to isolating the modes associated with the final periodic attractor from those yielding the

transient approach to the attractor, was able to very accurately identify 23 harmonics of the fundamental frequency in the periodic attractor, as seen in Fig.6. Instead, the FFT sideband artifacts produce a large amount of additional spurious frequencies. Indeed, with these spurious modes, the FFT ‘tries’ to describe the decaying behavior due to the actual modes exhibiting strictly negative growth rates, which cannot be computed by the FFT itself.

As a second comparison between FFT and HODMD, the current density data (already used for HODMD) in the timespan $200 \leq t \leq 300$, as in eq.(26), are treated via FFT, which identifies a large number of frequencies, all of them spurious, as seen in Fig.14–(b). In other words, not even the fundamental frequency is captured by the FFT in the present case, while HODMD was able to identify it well, together with 25 harmonics, as seen in Fig.12.

Summarizing, the performance of HODMD is superior to that of FFT in connection with both reliability and efficiency. In other words, HODMD identifies more clearly a larger number of the actual frequencies describing the periodic attractor. Besides, HODMD is able to separate the modes describing the permanent dynamics from their counterparts associated with the transient behavior.

IV. ANALYSIS OF THE PERIODIC ATTRACTOR VIA STKD

In this section, we further study the spatio-temporal structure of the periodic attractor and the underlying traveling wave dynamics of the electric field by using the STKD method. The periodic attractor has been computed from its transient by means of the HODMD method in Section III. As anticipated in Section I, the STKD method yields an expansion of the form

$$F(x, t) \simeq \sum_{(m,n) \in R_{ST}} a_{mn} u_{mn}^F e^{(\nu_m - i\kappa_m)x + i\omega_n t}, \quad (28)$$

where R_{ST} is the range of retained indices through spatio-temporal truncation; see eq.(B.8) in Appendix B. Note that, since we shall describe an attractor, all temporal growth rates have been set to zero. The spatial growth rates ν_m , instead, must be retained because the wave of the electric field is far from being periodic in x .

The average velocity c of the solitary wave of F can be estimated noticing that the latter

moves the length L in one period. Thus

$$c \simeq L/T_1 \simeq 0.44, \quad (29)$$

where the numerical values of L and T_1 are given in eqs.(8) and (23), respectively. The spatio-temporal diagram for the electric field in the periodic attractor that will be considered is shown in Fig.15–(a). Note that this plot does not coincide with its counterpart in Fig.2,

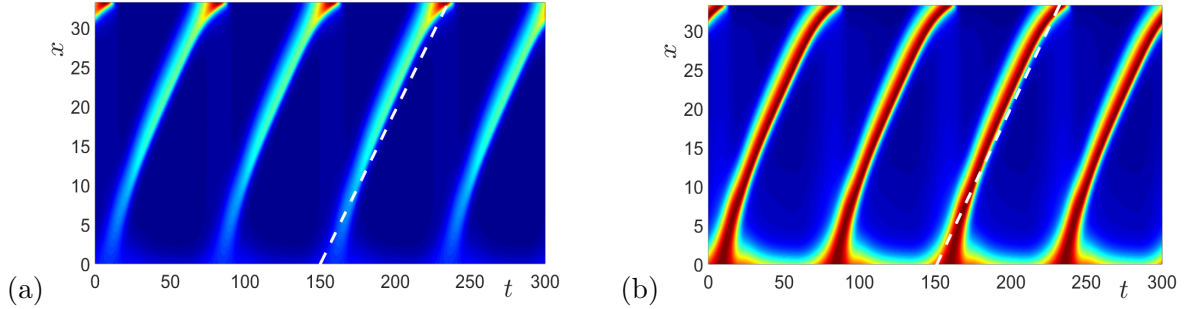


FIG. 15. Counterpart of Fig.2 for the electric field in the periodic attractor (a) and the scaled electric field defined in eq.(30) (b). In both plots, the dashed white line indicates the trajectory of a particle moving with the overall propagation velocity c defined in eq.(29). Thus, the slope of this line coincides with c .

where the whole evolution, including the transient stage, was shown. This diagram reveals two difficulties in connection with a STKD description through an expansion of the form (28):

- The (solitary) traveling wave is quite concentrated in both space and time. This means that the expansion (28) must be broadband for both the retained wavenumbers and frequencies, namely a fairly large number of relevant spatio-temporal modes is to be expected.
- The height of the wave significantly increases during its journey. This means that, in principle, very large, positive values of the spatial growth rate are to be expected.

The first difficulty cannot be overcome because it is inherent in the very nature of the solitary traveling wave. The second one, instead, can be alleviated by appropriately scaling the electric field as

$$F^{\text{scaled}}(x, t) = F(x, t) / \text{scale}(x), \quad (30)$$

where, as suggested by Fig.15–(a), the scale is defined as

$$\text{scale}(x) = \max_t F(x, t). \quad (31)$$

For illustration, this scale is plotted in Fig.16, which shows that it significantly varies from

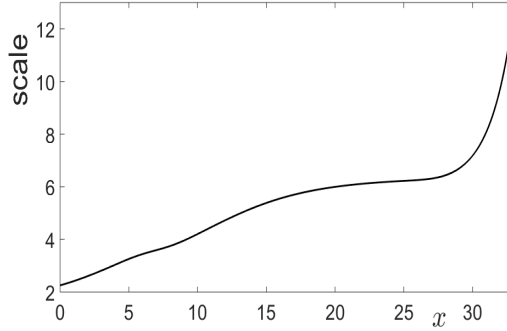


FIG. 16. The scale defined in eq.(31).

~ 2 at $x = 0$ to ~ 12 at $x = L$. Using such scale, the spatio-temporal diagram of F^{scaled} is given in Fig.15–(b), which shows a clearer traveling wave structure with F^{scaled} having a roughly constant intensity.

Now, the STKD method is applied to F^{scaled} with the following tunable STKD parameter values (see Appendix B)

$$\varepsilon_{\text{SVD}} = 5 \cdot 10^{-5}, \quad \varepsilon_{\text{DMD}} = 10^{-4}, \quad d^x = 1, \quad d^t = 25. \quad (32)$$

The reconstructed pattern shows a reasonable RRMS error, as defined in eq.(21), namely $\sim 2.75 \cdot 10^{-2}$ retaining 1038 spatio-temporal modes, which is a very large number, as expected. The temporal growth rates are all zero because the analyzed data correspond to the attractor. The (positive and negative) spatial growth rates, instead, are $\sim 10^{-2}$ in absolute value. This was to be expected because, as anticipated, the pattern is far from being periodic in the spatial direction. The associated *dispersion diagram* is plotted in Fig.17. As can be seen, most relevant points in this diagram are contained in a rhomboid, whose largest diagonal is indicated by a thick dashed line. The slope of this diagonal is $\omega/\kappa \simeq c$, where c is the overall propagation velocity, given in eq.(29).

Summarizing, even in this very demanding situation, the STKD method, with an appropriately large number of spatio-temporal modes, is able to describe reasonably well the present solitary traveling wave, estimating its overall propagation velocity. The CPU time

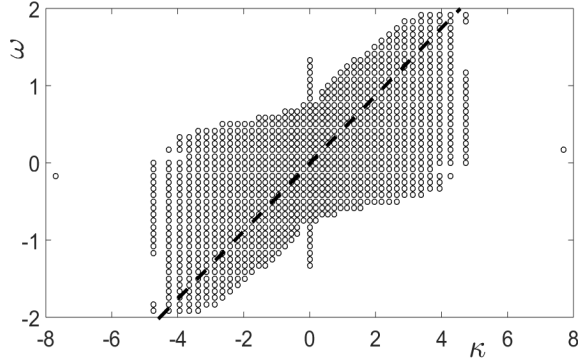


FIG. 17. Dispersion diagram resulting from the application of the STKD method to the scaled electric field in eq.(30) in the periodic attractor, using the tunable parameters in eq.(32).

required by the application of the STKD method is ~ 7 CPU seconds, using the standard PC described at the end of Section I. However, the analysis in this section shows that, in principle, the STKD method is not appropriate to construct data-driven ROMs for the present problem. This is due to the large number of spatio-temporal modes that should be retained, which would increase the CPU time required by the online operation of the ROM. Thus, in the next section, the proposed data-driven ROM will be constructed using the HODMD method, which involves a moderate number of temporal modes.

V. A PRELIMINARY VERSION OF A HODMD-BASED DATA-DRIVEN ROM

In the previous two sections, we have used data obtained upon numerical integration of the superlattice equations to reconstruct and analyze the structure of the underlying spatio-temporal pattern in different ways. Let us now use the analysis in Section III to *construct offline* a data-driven ROM, able to *simulate online* the superlattice periodic attractor for continuous values of one or more parameters in a given parameter range. Here, for simplicity, we restrict the discussion to only one parameter, namely the *contact conductivity*, $\sigma > 0$. The extension of the proposed data-driven ROM to cases in which more than one parameter is involved is straightforward, as is the extension to other related dynamical systems. However, this is well beyond the scope of the present paper.

Let us consider the parameter range

$$0.3 \leq \sigma \leq 0.7 \tag{33}$$

and the following *basic values* of the contact conductivity

$$\sigma_1 = 0.3, \quad \sigma_2 = 0.4, \quad \sigma_3 = 0.5, \quad \sigma_4 = 0.6, \quad \sigma_5 = 0.7. \quad (34)$$

The remaining parameters are kept fixed to the values already used in Section III. The algorithm of the proposed, novel data-driven ROM follows three steps.

1. For each basic value of σ in eq.(34), the periodic attractor is computed running the numerical solver in the time interval $0 \leq t \leq 300$.
2. For each basic value of σ in eq.(34), the HODMD method is applied to snapshots in the timespan $200 \leq t \leq 300$ using the following parameter values

$$\varepsilon_{\text{SVD}} = 10^{-7}, \quad \varepsilon_{\text{DMD}} = 5 \cdot 10^{-4}, \quad d = 35, \quad (35)$$

which have been chosen after a slight calibration. Since the number of computed modes varies from 55 to 57, depending on the case, 55 modes are retained in all cases for consistency. In this way, the RRMS error in the reconstruction of the periodic orbit for the current density and the electric field is $\sim 10^{-4}$ and $\sim 10^{-3}$, respectively, while all growth rates are smaller than 10^{-4} in absolute value. For each case, the involved fundamental frequency, amplitudes, and modes are stored.

3. For any *new value* of σ in the range (33), the associated fundamental frequency, amplitudes, and modes are calculated upon appropriate interpolation (see below), using the fundamental frequencies, amplitudes, and modes stored for the basic values of σ in eq.(34). This allows to reconstruct the *new attractor* using the HODMD expansions (18)-(19).

Note that steps 1–2 of the algorithm correspond to the *offline* stage of the ROM, namely the preprocess needed at the outset to construct all ingredients, while step 3 implements the *online* operation of the ROM, yielding the desired output. We also recall that in the expansions (18)-(19), which are reported here for convenience,

$$J(t) \simeq \sum_{p=-P}^P a_p u_p^J e^{i p \omega_1 t}, \quad (36)$$

$$F(x_i, t) \simeq \sum_{p=-P}^P a_p u_p^F(x_i) e^{i p \omega_1 t}, \quad (37)$$

the amplitudes a_p , the fundamental frequency ω_1 , and the number P of positive and negative harmonics are common. Since data are real, the various terms must be conformed in complex conjugate pairs. Namely, expansions (36)-(37) are invariant under the transformations

$$p \rightarrow -p, \quad u_p^J \rightarrow \overline{u_p^J}, \quad u_p^F \rightarrow \overline{u_p^F}, \quad (38)$$

where the overline denotes the complex conjugate. In addition, since the considered snapshots are as in eq.(14), expansions (36)-(37) can be recast in vector form, similar to eq.(2), where the vectors appearing in its left and right-hand sides are given by

$$\mathbf{q}(t) = \begin{bmatrix} J(t) \\ F(x_1, t) \\ F(x_2, t) \\ \vdots \\ F(x_I, t) \end{bmatrix} \quad \text{and} \quad \mathbf{u}_p = \begin{bmatrix} u_p^J \\ u_p^F(x_1) \\ u_p^F(x_2) \\ \vdots \\ u_p^F(x_I) \end{bmatrix}, \quad (39)$$

for $p = -P, \dots, P$.

Before discussing how step 3 of the proposed algorithm is performed, an important aspect must be pointed out. Indeed, efficient interpolation of the computed modes requires that these be appropriately synchronized. Note that *synchronization* was not necessary in Section III since all data came from a single run of the numerical solver, namely a unique periodic attractor (from prescribed initial condition and parameter values) was computed and compared to its approximations in the same timespan. If, instead, the numerical solver were run several times, using different initial conditions and/or comparing the outcomes in distinct timespans, then the resulting asymptotic states would not be automatically synchronized, namely they would show *time shifts* among each other. Likewise, in the present case, the modes for the various basic values of σ come from different simulations of the numerical solver and need to be synchronized too. Synchronization means *shifting* the time variable appearing in eqs.(36)-(37) as

$$t \rightarrow t + t_{\text{shift}}, \quad (40)$$

for an appropriate value of t_{shift} , in order to make the expansions for all considered values of the parameter consistent among each other. Note that applying the action (40) also requires

redefining the modes as

$$u_p^J \rightarrow u_p^J e^{-i p \omega_1 t_{\text{shift}}}, \quad u_p^F \rightarrow u_p^F e^{-i p \omega_1 t_{\text{shift}}}. \quad (41)$$

The time shift can be calculated in various ways. In the present method, it is computed by synchronizing the fundamental mode for the current density in eq.(36), u_1^J , which is done defining

$$t_{\text{shift}} = \frac{\log(u_1^J/|u_1^J|)}{i \omega_1}. \quad (42)$$

Hence, with this selection of the time shift and after performing the transformations (40)-(41), u_1^J becomes real and the associated monochromatic oscillation is

$$a_1 \left[u_1^J e^{i \omega_1 t} + \bar{u}_1^J e^{-i \omega_1 t} \right] = a_1 |u_1^J| \cos(\omega_1 t). \quad (43)$$

For convenience, the synchronized HODMD reconstructions of the periodic attractors will be compared in the timespan

$$-T_1 \leq t \leq T_1 \quad (44)$$

in all simulations below, where the period T_1 of the orbit is defined in terms of the fundamental frequency as in eq.(23). In order to illustrate the synchronization effect, we consider the largest basic value of σ defined in eq.(34), namely $\sigma = \sigma_5 = 0.7$. For this case, the fundamental frequency and period are

$$\omega_1 = 0.085904 \quad \text{and} \quad T_1 = 73.142, \quad (45)$$

both with six exact significant digits, while the time shift is

$$t_{\text{shift}} = -22.696. \quad (46)$$

Using these values, the synchronized reconstruction of the current density and the electric field in the time interval (44) is plotted in Fig.18. For the smallest basic value of σ defined in eq.(34), namely $\sigma = \sigma_1 = 0.3$, the fundamental frequency is $\omega_1 = 0.085155$ and the associated period is $T_1 = 73.786$, both with six exact significant digits. Note that these values are fairly close to their counterparts for σ_5 . Instead, the time shift is now $t_{\text{shift}} = -33.417$, which is not close to its counterpart for σ_5 . Also, the synchronized reconstruction of the current density and the electric field in the time interval (44), plotted in Fig.19, is quite different from its counterpart for σ_5 , especially for the current density, as comparison with

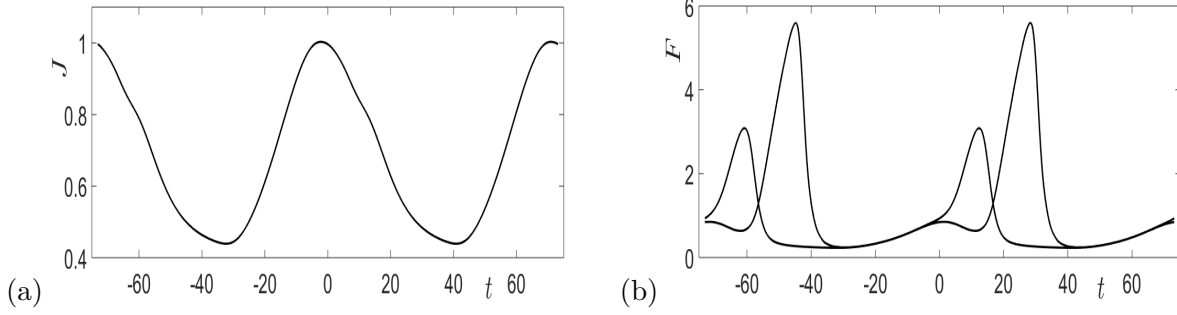


FIG. 18. Temporal evolution of the current density (a) and the electric field at $x = \tilde{x}_1$ and $x = \tilde{x}_2$ as defined in eq.(12) (b), for the synchronized HODMD reconstruction of the periodic attractor corresponding to $\sigma = \sigma_5 = 0.7$, in the time interval (44).

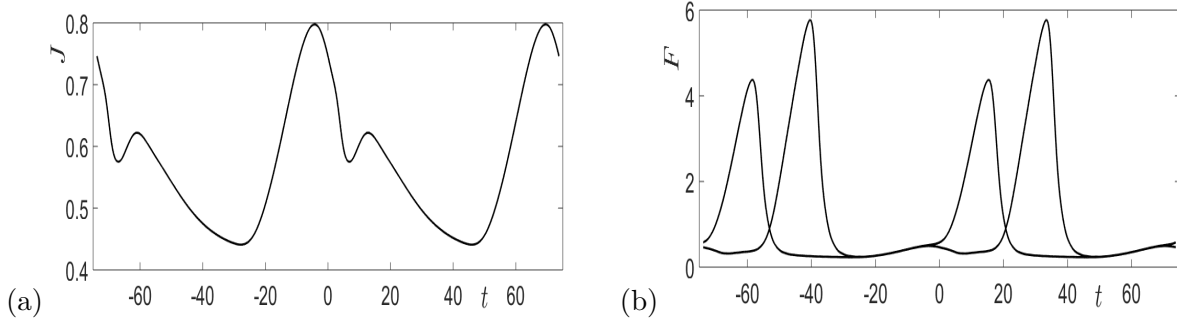


FIG. 19. Counterpart of Fig.18 for the periodic attractor corresponding to $\sigma = \sigma_1 = 0.3$.

Fig.18 shows. Thus, we may guess that the fundamental frequency is fairly constant for the basic values of σ in eq.(34), but the periodic orbit varies significantly.

Let us now discuss how the proposed HODMD-based data-driven ROM is able to efficiently simulate the system response for any *new* value of σ in the range (33). In other words, let us clarify how *interpolation* is performed in step 3 of the introduced algorithm. The new value of the fundamental frequency is computed upon spline interpolation using the values of ω_1 for the basic values of σ in eq.(34). Interpolation of the spatial modes could be performed point-by-point by, e.g., splines. However, this strategy would be computationally inefficient. A more efficient interpolation procedure is developed as follows. To begin with, the retained modes defined in eq.(39) are first synchronized and then scaled with the mode amplitudes. Namely, all synchronized modes are scaled as

$$\mathbf{u}_p^* = a_p \mathbf{u}_p, \quad \text{with } p = -P, \dots, P, \quad (47)$$

for all basic values of σ in eq.(34). The resulting modes could be organized in a third-order

tensor, whose components are given by

$$T_{ipq} = u_{ip,q}^*, \quad (48)$$

where $i = 1, \dots, I+1$ labels the mode component, $p = -P, \dots, P$ stands for the mode index, and $q = 1, \dots, Q$ indicates the basic value of σ . Note that, in the present case, the tensor \mathbf{T} will have dimension equal to $(I+1) \times (2P+1) \times Q = 482 \times 55 \times 5$. This tensor could be treated using the HOSVD tensor decomposition [40] combined with 1D interpolation, as explained in [41]. However, for simplicity, here we unfold the tensor \mathbf{T} into a matrix \mathbf{A} by collecting together the first two indices appearing in eq.(48), i and p , into a single index, denoted as l . The matrix \mathbf{A} is then dimension-reduced using truncated *singular value decomposition* (SVD) [42], requiring that the RRMS error of the reconstruction be smaller than a threshold. This yields the approximated matrix with components

$$A^{\text{approx}}(l, q) = \sum_{l'=1}^{L'} s_{l'} U_{ll'} V_{ql'}, \quad (49)$$

where $s_{l'}$ are the retained singular values, while $U_{l'}$ and $V_{l'}$ are the corresponding left and right SVD modes, respectively. Note that, for $q = 1, \dots, Q$, the two sides of this equation account for the $Q = 5$ basic values of σ in eq.(34). Thus, eq.(49) can be rewritten as

$$A_l^{\text{approx}}(\sigma_q) = \sum_{l'=1}^{L'} s_{l'} U_{ll'} V_{l'}(\sigma_q). \quad (50)$$

Now, for each $l' = 1, \dots, L'$, 1D spline interpolation can be applied to $V_{l'}(\sigma_q)$ to compute this quantity for the new value of σ , say σ^{new} . Hence, from eq.(50) we get

$$A_l^{\text{approx}}(\sigma^{\text{new}}) = \sum_{l'=1}^{L'} s_{l'} U_{ll'} V_{l'}(\sigma^{\text{new}}). \quad (51)$$

More details about combining SVD with interpolation can be found in [43, 44]. Finally, splitting the index l into the original indices, i and p , which were collected together in the matrix \mathbf{A} , and invoking eq.(47) give the scaled, synchronized modes for the new value of σ , namely

$$\mathbf{u}_p^{*\text{new}}, \quad \text{for } \sigma = \sigma^{\text{new}}. \quad (52)$$

Using these modes, the amplitudes and the original normalized modes (exhibiting unit RMS norm) for $\sigma = \sigma^{\text{new}}$ are obtained from eq.(52) as

$$a_p^{\text{new}} = \frac{\|\mathbf{u}_p^{*\text{new}}\|_2}{\sqrt{I+1}}, \quad \mathbf{u}_p^{\text{new}} = \frac{\mathbf{u}_p^{*\text{new}}}{a_p^{\text{new}}}, \quad \text{for } \sigma = \sigma^{\text{new}}, \quad (53)$$

and the associated synchronized HODMD reconstructions of the current density and the electric field are readily obtained via the expansions (36)-(37).

In order to highlight the accuracy of the data-driven ROM, we consider two very demanding test cases corresponding to values of σ near the end-points of the parameter range (33). For $\sigma^{\text{new}} = 0.65$, the outcome of the ROM is compared in Fig.20 with its ‘exact’

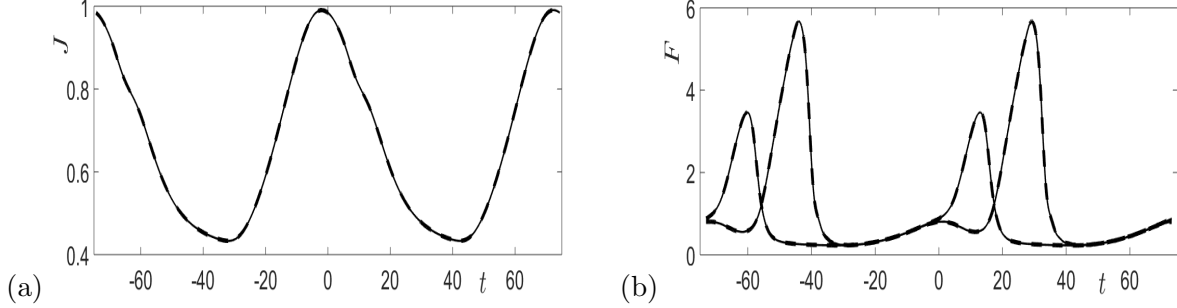


FIG. 20. Synchronized attractor for $\sigma^{\text{new}} = 0.65$, in the time interval (44), for the current density (a) and the electric field at $x = \tilde{x}_1$ and $x = \tilde{x}_2$ as defined in eq.(12) (b). In these plots, the ‘exact’ evolution is displayed in thin solid lines, while the outcome of the HODMD-based data-driven ROM is depicted with thick dashed lines.

counterpart computed by the numerical solver. Note that the reference and approximated periodic attractors are plot-indistinguishable. For $\sigma^{\text{new}} = 0.35$, the counterpart of Fig.20 is Fig.21, where it can be seen that the approximated and ‘exact’ periodic orbits are again

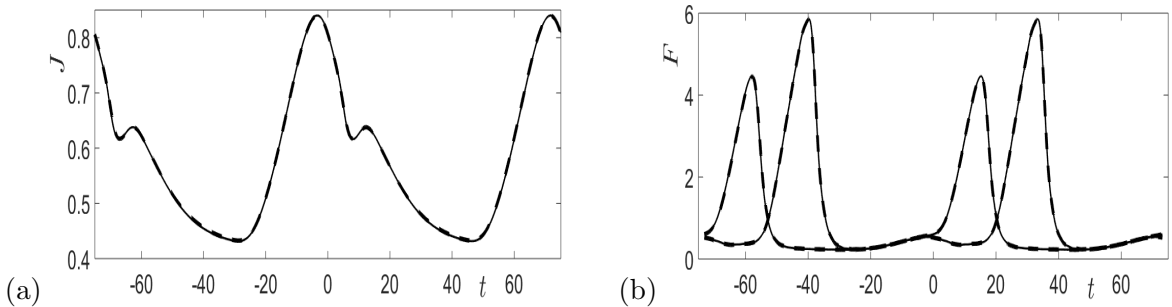


FIG. 21. Counterpart of Fig.20 for $\sigma^{\text{new}} = 0.35$.

plot-indistinguishable. For other values of the parameter σ in the range (33), the outcome of the HODMD-based data-driven ROM is either equally good or even better. Due to the large computational cost of the numerical solver, the CPU time needed to generate the considered snapshots is ~ 2 CPU hours. Instead, the cost of the remaining HODMD tasks required

in the offline stage of the ROM is much smaller, namely ~ 30 CPU seconds. On the other hand, the online operation of the ROM, for any new value of σ , is quite cheap, namely it takes ~ 0.5 CPU seconds.

VI. CONCLUDING REMARKS

We have studied self-oscillations of the current through a one miniband semiconductor superlattice and the associated electric field waves by using the HODMD and STKD data processing methods. The properties of the self-oscillations (i.e., their spectrum comprising growth rate vs. frequency, wave shape, and propagation) depend on the device configuration and, in particular, on the conductivity of the injecting contact.

Firstly, we have applied the HODMD tool to data of a complete numerical simulation that includes both the transient stage and the final time periodic attractor of the current self-oscillations. As a result, we have identified the attractor and separated it from the purely decaying dynamics of the transient stage. We have also performed additional test cases in which we reconstruct the periodic attractor by using snapshots in various limited timespans. In particular, we are able to approximate well the attractor using snapshots taken during the transient stage. This last approach is important because it decreases the computational cost of calculating the snapshots, while preserving the physical properties within a satisfactory accuracy.

Secondly, we have used the STKD method to characterize fairly well the electric field traveling pulse and its average propagation velocity. This is a challenging endeavor because the pulse wave is quite localized in both space and time, which implies that the STKD description involves a large number of spatio-temporal modes.

In addition, we have constructed a preliminary version of a novel HODMD-based data-driven reduced order model for the superlattice dynamics. This ROM enables very fast online simulations of the device response over a range of values of the contact conductivity. For each test case, the online ROM operation requires only ~ 0.5 CPU seconds, which is much smaller than the computational cost needed by the considered standard numerical solver (namely ~ 20 CPU minutes). Thus, in this context, the data-driven ROM divides the computational effort by a factor ~ 2500 . The drawback of our preliminary version is that the ROM offline preprocess takes ~ 2 CPU hours. However, most of this CPU time

is due to the required runs to calculate the input snapshots. Hence, it could be drastically reduced by replacing the standard numerical solver by a low-dimensional model based on POD and Galerkin projection of the governing equations. This improvement is far beyond the scope of the present work and will be pursued elsewhere. Finally, it is worth remarking that an extension of the developed data-driven approach to analyses involving more than one parameter would be straightforward.

Our results show that appropriate data processing tools can be used to *(i)* uncover the dynamics underlying a physical system, and *(ii)* construct purely data-driven ROMs for a parametric study of the involved mechanisms. For semiconductor superlattices, these methods could be particularly valuable when a tilted external magnetic field is present [11–14]. In this case, the periodic motion of charge dipole waves is 2D and the numerical computations needed to explore parameter regions are much more costly [14]. Hence, the techniques presented in this paper could be very helpful indeed.

ACKNOWLEDGMENTS

The authors are indebted to two anonymous referees for some useful comments and suggestions on an earlier version of the manuscript. This work has been supported by the FEDER / Ministerio de Ciencia, Innovación y Universidades – Agencia Estatal de Investigación, under grants TRA2016-75075-R, MTM2017-84446-C2-2-R, and PID2020-112796RB-C22, and by the Madrid Government (Comunidad de Madrid-Spain) under the Multiannual Agreement with UC3M in the line of Excellence of University Professors (EPUC3M23) and in the context of the V PRICIT (Regional Programme of Research and Technological Innovation).

Appendix A: The HODMD method

The *higher order dynamic mode decomposition* (HODMD) and the *spatio-temporal Koopman decomposition* (STKD) are summarized in this and the following appendices. These tools have proven to give good results in uncovering the nature of spatio-temporal patterns, from either numerical or experimental data, in a variety of dynamical systems of scientific and industrial interest [45], including, e.g., PIV wind tunnel measurements [46, 47], wind

turbine operation [48, 49], aircraft flight flutter testing [50, 51], basic fluid dynamics [52], and pattern-forming systems [53]. See also [26] for a reader-friendly description of the HODMD and STKD methods and some of their applications, as well as for specific MATLAB implementations of their algorithms.

The HODMD method [24] is now briefly detailed. The outcome of this technique is a discrete expansion of the form

$$\mathbf{q}_k \equiv \mathbf{q}(t_k) \simeq \sum_{n=1}^N a_n \mathbf{u}_n e^{(\delta_n + i\omega_n) t_k}, \quad (\text{A.1})$$

with $t_k = (k-1) \Delta t$, for $k = 1, \dots, K$. Here, \mathbf{q}_k are *snapshots* for the involved state variable at Δt -spaced values of time, $a_n > 0$ are real *amplitudes*, \mathbf{u}_n are conveniently normalized (generally complex) *modes*, and δ_n and ω_n are the associated *growth rates* and *frequencies*, respectively. HODMD is an improvement of standard dynamic mode decomposition (DMD) [38, 39]. By improving standard DMD we mean that, conveniently calibrated, HODMD yields robust results when standard DMD fails. Indeed, the latter can only cope with cases in which the spectral complexity coincides with the spatial complexity, while HODMD gives good results also when the spatial complexity is strictly smaller than the spectral complexity (see below). On the other hand, HODMD could be compared to FFT and well-known improvements of FFT, such as the power spectral density [54] and the so-called Laskar method [55, 56]. However, compared to FFT and its improvements, HODMD exhibits two main advantages, since (i) it provides not only the frequencies but also the associated growth rates and (ii) it requires a smaller amount of data, in a shorter timespan. Furthermore, once the expansion (A.1) has been obtained, replacing t_k by t readily yields the continuous expansion (2), which can be seen as an analytical description of the dynamics associated with the given data (i.e., those provided by the dynamical system behind the data).

Without loss of generality, it is assumed that the coefficients $\delta_n + i\omega_n$ appearing in the exponential of eq.(A.1) are different from each other. Indeed, if some of them coincide, they can be collected in a single term. The rank (or approximate rank) of the set of modes, \mathbf{u}_n , denoted by M , is known as the *spatial complexity*, while the number of terms appearing in eq.(A.1), N , is the *spectral complexity*, which obviously verifies $N \geq M$. Note that the amplitudes could have been absorbed into the modes. However, isolating a_n and \mathbf{u}_n by normalizing the latter such that, e.g., they exhibit unit RMS norm, the amplitudes give a quantitative measure of the contribution of the various modes. This helps to identify the

dominant modes as those exhibiting the largest amplitudes. Also, retaining only those terms whose amplitudes are larger than a desired threshold permits appropriate *truncation* of the expansion. In any event, the expansion (2) (the continuous counterpart of eq.(A.1)) is only an approximation of $\mathbf{q}(t)$ for various reasons, including errors in the given data (which can be significant in experimental data), truncation, and computational errors in the calculation of the amplitudes, modes, growth rates, and frequencies. We remark that HODMD gives the expansion (2) in a purely data-driven fashion, namely not relying on the governing equations, but using only a limited amount of associated data.

The derivation of eq.(A.1) is now summarized for the case used in this paper. See [24] for further details and more general versions of the HODMD method that allow for treating spatially multi-dimensional data and filtering noisy artifacts in experimental data. To begin with, the snapshots \mathbf{q}_k are assumed to be vectors of size I and are organized as columns of a *snapshot matrix*, namely

$$\mathbf{Q}_1^K = [\mathbf{q}_1, \mathbf{q}_2, \dots, \mathbf{q}_K]. \quad (\text{A.2})$$

Then, the snapshots are dimension-reduced by applying truncated SVD [42] to the $I \times K$ -snapshot matrix \mathbf{Q}_1^K , which yields

$$\mathbf{Q}_1^K \simeq \mathbf{U} \mathbf{\Sigma} \mathbf{V}^\top \equiv \mathbf{U} \hat{\mathbf{Q}}_1^K \quad (\text{or } \mathbf{q}_k = \mathbf{U} \hat{\mathbf{q}}_k), \quad (\text{A.3})$$

where the $M \times K$ -matrix $\hat{\mathbf{Q}}_1^K = \mathbf{\Sigma} \mathbf{V}^\top$ is known as the *dimension-reduced snapshot matrix* and its columns, whose size is M , are the *dimension-reduced snapshots*, $\hat{\mathbf{q}}_k$. The number of retained singular values, $M \leq I$, is precisely the spatial complexity and is determined by a (tunable) *dimension reduction threshold*, ε_{SVD} , requiring that the RRMS error of the approximation, as defined in eq.(21), be smaller than ε_{SVD} . Note that this error is easily computed in terms of the singular values using well-known SVD formulae [42].

As a second step, the counterpart of the expansion (A.1) for the reduced snapshots, namely

$$\hat{\mathbf{q}}_k \simeq \sum_{n=1}^N a_n \hat{\mathbf{u}}_n e^{(\delta_n + i\omega_n)t_k} \quad \text{for } k = 1, \dots, K, \quad (\text{A.4})$$

is derived as follows. For the reduced snapshots, standard DMD relies on the assumption

$$\hat{\mathbf{q}}_{k+1} \simeq \hat{\mathbf{R}} \hat{\mathbf{q}}_k \quad \text{for } k = 1, \dots, K, \quad (\text{A.5})$$

where the $M \times M$ matrix $\hat{\mathbf{R}}$ (the reduced *Koopman matrix*) is computed from the dimension-reduced snapshots via the pseudo-inverse [24]. The non-zero eigenvalues of the reduced

Koopman matrix, μ_n , give the growth rates and frequencies appearing in eq.(A.4) as

$$\delta_n + \mathrm{i}\omega_n = \frac{1}{\Delta t} \log(\mu_n) \quad \text{for } n = 1, \dots, N, \quad (\text{A.6})$$

while the (conveniently normalized) associated eigenvectors $\hat{\mathbf{u}}_n$ yield the reduced modes. The mode amplitudes a_n are computed via least-squares fitting between the two sides of eq.(A.4). This computation is similar to what is done in optimized DMD [57]. Using the mode amplitudes computed in this way, the reduced expansion (A.4) is finally truncated retaining only those terms such that

$$\frac{a_n}{\max\{a_n\}} > \varepsilon_{\text{DMD}}, \quad (\text{A.7})$$

for some (small) tunable *mode truncation threshold* ε_{DMD} .

Once eq.(A.4) has been obtained, pre-multiplying it by the matrix \mathbf{U} appearing in eq.(A.3) gives a first version of the expansion (A.1), where

$$\mathbf{u}_n = \mathbf{U} \hat{\mathbf{u}}_n. \quad (\text{A.8})$$

In fact, the amplitudes and modes computed in eqs.(A.7)-(A.8) are jointly rescaled (namely, scaled again after the previous implicit scalings performed above, to scale the right SVD modes with the singular values in eq.(A.3) and to normalize the reduced modes $\hat{\mathbf{u}}_n$ appearing in eq.(A.4)), requiring that the modes exhibit unit RMS norm while preserving the product $a_n \mathbf{u}_n$. It is precisely these rescaled amplitudes and modes that are used in the right-hand side of eq.(A.1), while the growth rates and frequencies are as computed for the reduced expansion (A.4), according to eq.(A.6). Note that, since the growth rate/frequency pairs are all different from each other, invoking eq.(A.6), the eigenvalues μ_n are also different and the eigenvectors $\hat{\mathbf{u}}_n$ are linearly independent. This means that, in the present case, $M = N$. In other words, in standard DMD, the spatial and spectral complexities coincide, as anticipated.

The general case $N \geq M$ is dealt with via HODMD, in which the assumption (A.5) is replaced by

$$\hat{\mathbf{q}}_{k+d} \simeq \hat{\mathbf{R}}_1 \hat{\mathbf{q}}_{k+d-1} + \hat{\mathbf{R}}_2 \hat{\mathbf{q}}_{k+d-2} + \dots + \hat{\mathbf{R}}_d \hat{\mathbf{q}}_k, \quad (\text{A.9})$$

which increases the spectral complexity, as seen below. For convenience, the assumption (A.9) is rewritten as

$$\tilde{\mathbf{q}}_{k+1} \simeq \tilde{\mathbf{R}} \tilde{\mathbf{q}}_k \quad \text{for } k = 1, \dots, K - d + 1, \quad (\text{A.10})$$

where the *enlarged snapshots* $\tilde{\mathbf{q}}_k$ are defined in terms of the reduced snapshots $\hat{\mathbf{q}}_k$ as

$$\tilde{\mathbf{q}}_k \equiv \begin{bmatrix} \hat{\mathbf{q}}_k \\ \hat{\mathbf{q}}_{k+1} \\ \vdots \\ \hat{\mathbf{q}}_{k+d-2} \\ \hat{\mathbf{q}}_{k+d-1} \end{bmatrix}. \quad (\text{A.11})$$

The index $d \geq 1$ appearing in eqs.(A.9) and (A.11) is tunable in this method. Comparing eq.(A.10) with eq.(A.5) suggests to apply standard DMD to the enlarged snapshots, which gives

$$\tilde{\mathbf{q}}_k \simeq \sum_{n=1}^N a_n \tilde{\mathbf{u}}_n e^{(\delta_n + i\omega_n)t_k} \quad \text{for } k = 1, \dots, K - d + 1. \quad (\text{A.12})$$

In this application of standard DMD, the dimension reduction threshold, ε_{SVD} , coincides with its counterpart in the first dimension reduction of the original snapshots. Once the expansion (A.12) has been calculated, invoking eq.(A.11), the first M components of the vectors appearing in the left and right-hand sides of eq.(A.12) lead to an expansion of type (A.4) for the reduced snapshots $\hat{\mathbf{q}}_k$. The mode amplitudes a_n are recalculated via least-squares fitting between the two sides of eq.(A.4). Truncating (using a tunable threshold ε_{DMD}) the latter expansion and pre-multiplying it by the matrix \mathbf{U} appearing in eq.(A.3) lead to the expansion (A.1) for the original snapshots. Finally, as explained for the standard DMD right after eq.(A.8), the amplitudes and modes in the last expansion are jointly rescaled requiring that the modes exhibit unit RMS norm while preserving the product $a_n \mathbf{u}_n$.

The HODMD method described above is called *DMD- d algorithm*. Obviously, for $d = 1$, the DMD-1 algorithm reduces to standard DMD. Also, for appropriate $d > 1$, the DMD- d algorithm is able to cope with arbitrary spatial and spectral complexities. A MATLAB solver for the DMD- d algorithm can be found in [26, 58]. The algorithm depends on some tunable parameters, whose selection is commented in the following (see [24] for further details).

- In order to avoid aliasing [59], the temporal distance between snapshots, Δt , must be much smaller (say, five times smaller) than the smallest period involved in the expansion (A.1). Likewise, the total timespan where the snapshots are selected, $t_K - t_1$, must be somewhat larger (say, 1.5 times as large) than the largest involved period. These values define the total number of considered snapshots, K .

- For ‘clean’ snapshots, the dimension reduction and mode truncation thresholds (ε_{SVD} and ε_{DMD} , respectively) can be comparable to each other and quite small. This occurs in the applications described in the present paper. Decreasing both of them typically increases the accuracy of the obtained HODMD expansion, but it also increases the number of retained modes. In other words, a trade-off is needed to select these thresholds. Let us mention that, for noisy snapshots obtained from experimental data, ε_{SVD} should be taken as comparable to the noise level. This helps to filter noise due to well-known noise-filtering properties of the method [46].
- The index d appearing in eqs.(A.9) and (A.11) allows to deal with *time-lagged* snapshots and can be chosen to somewhat minimize the RRMS error (as defined in eq.(21)) of the approximation of the reduced snapshots, defined in (A.4). It must be noted that d scales with K , namely, when doubling K , d must be doubled as well.
- The algorithm is quite robust in connection with the tunable parameters ε_{SVD} , ε_{DMD} , and d . In particular, the plot of the approximation RRMS error vs. d is fairly flat near the optimal value, which means that the selection of d is not critical.

Appendix B: The STKD method

For spatially 1D dynamics, the outcome of the STKD method is a discrete expansion of the form [25]

$$q(x_i, t_k) \simeq \sum_{m=1}^M \sum_{n=1}^N a_{mn} u_{mn} e^{(\nu_m - i\kappa_m)x_i + (\delta_n + i\omega_n)t_k}, \quad (\text{B.1})$$

where $t_k = (k - 1)\Delta t$, for $k = 1, \dots, K$, and the I discrete values of x , required to be equispaced, are defined as

$$x_i = (i - 1)\Delta x, \quad \text{for } i = 1, \dots, I. \quad (\text{B.2})$$

Here, $q(x_i, t_k)$ are the components of snapshots for the involved state variable, $a_{mn} > 0$ are real *amplitudes*, u_{mn} are normalized (generally complex) *modes*, ν_m and δ_n are *spatial* and *temporal growth rates*, respectively, κ_m are *wavenumbers*, and ω_n are *frequencies*. The derivation of the discrete expansion (B.1) is now summarized for the case considered in this paper, in which a scalar state variable and a single longitudinal coordinate x are involved. Full details can be found in [25], where more general cases are considered, namely involving

a vector state variable, more than one longitudinal coordinates, or additional transverse coordinates.

As a first step, the snapshots appearing in the left-hand side of the expansion (B.1) are organized in a $I \times K$ -snapshot matrix, as defined in eq.(A.2). This matrix is dimension-reduced via truncated SVD according to a *dimension reduction threshold*, ε_{SVD} . After truncation, the snapshot matrix is approximated as

$$\mathbf{Q}_1^K \simeq \mathbf{U} \mathbf{\Sigma} \mathbf{V}^\top \equiv (\hat{\mathbf{Q}}^x)^\top \hat{\mathbf{Q}}^t, \quad (\text{B.3})$$

where

$$\hat{\mathbf{Q}}^x = \sqrt{\mathbf{\Sigma}} \mathbf{U}^\top \text{ and } \hat{\mathbf{Q}}^t = \sqrt{\mathbf{\Sigma}} \mathbf{V}^\top. \quad (\text{B.4})$$

These matrices are called the *reduced spatial* and *temporal snapshot matrices*, respectively, and their columns, \hat{q}_i^x and \hat{q}_k^t , are called the *reduced spatial* and *temporal snapshots*, respectively. Comparison of eqs.(B.4) and (A.3) shows that, while the SVD singular values are used in the HODMD method to scale the reduced temporal snapshots, here they are equidistributed between the reduced spatial and temporal snapshots, which are thus scaled by the square root of the SVD singular values.

As a second step, the DMD- d algorithm described in Appendix A is applied to both the reduced spatial snapshots and the reduced temporal snapshots, using appropriate indices d^x and d^t (which do not necessarily coincide), respectively. For simplicity, we can use a dimension reduction threshold, ε_{SVD} , equal to its counterpart in the first dimension reduction step leading to eq.(B.4). In addition, we can consider a common mode truncation threshold, ε_{DMD} , when applying HODMD to the reduced spatial and temporal snapshots. It follows that

$$\hat{q}_i^x \simeq \sum_{m=1}^M \hat{a}_m^x \hat{u}_m^x e^{(\nu_m - i\kappa_m)x_i} \quad \text{for } i = 1, \dots, I, \quad (\text{B.5})$$

$$\hat{q}_k^t \simeq \sum_{n=1}^N \hat{a}_n^t \hat{u}_n^t e^{(\delta_n + i\omega_n)t_k} \quad \text{for } k = 1, \dots, K. \quad (\text{B.6})$$

Substituting these expansions into the columns of the matrices $\hat{\mathbf{Q}}^x$ and $\hat{\mathbf{Q}}^t$ appearing in eq.(B.3) yields the STKD expansion (B.1), with

$$a_{mn} = |\hat{a}_m^x \hat{a}_n^t \hat{u}_m^x \hat{u}_n^t|, \quad u_{mn} = \hat{a}_m^x \hat{a}_n^t \hat{u}_m^x \hat{u}_n^t / a_{mn}. \quad (\text{B.7})$$

Note that the (complex) scalar modes u_{mn} exhibit unit absolute value, as required. Finally, truncation is performed in the expansion (B.1) by retaining only those terms such that

$$\frac{a_{mn}}{\max\{a_{mn}\}} > \varepsilon_{\text{DMD}}, \quad (\text{B.8})$$

where the threshold ε_{DMD} coincides with the mode truncation threshold previously set to truncate the expansions (B.5)-(B.6).

-
- [1] L. Esaki and R. Tsu, Superlattice and negative differential conductivity in semiconductors, *IBM J. Res. Dev.* **14**, 61 (1970).
 - [2] J. Feldmann, K. Leo, J. Shah, D.A.B. Miller, J.E. Cunningham, T. Meier, G. von Plessen, A. Schulze, P. Thomas, and S. Schmitt-Rink, Optical investigation of Bloch oscillations in a semiconductor superlattice, *Phys. Rev. B* **46**, 7252 (1992).
 - [3] L.L. Bonilla, M. Álvaro, and M. Carretero, Theory of spatially inhomogeneous Bloch oscillations in semiconductor superlattices, *Phys. Rev. B* **84**, 155316 (2011).
 - [4] L.L. Bonilla and H.T. Grahn, Nonlinear dynamics of semiconductor superlattices, *Rep. Prog. Phys.* **68**, 577 (2005).
 - [5] D.O. Winge, E. Dupont, and A. Wacker, Ignition of quantum cascade lasers in a state of oscillating electric field domains, *Phys. Rev. A* **98**, 023834 (2018).
 - [6] S.Y. Lee, M. Choo, S. Jung, and W. Hong, Optically transparent nano-patterned antennas: A review and future directions, *Appl. Sci.* **8**, 901 (2018).
 - [7] L.L. Bonilla and S.W. Teitsworth, Nonlinear wave methods for charge transport, *Wiley-VCH, Weinheim*, 2010.
 - [8] W. Li, I. Reidler, Y. Aviad, Y. Huang, H. Song, Y. Zhang, M. Rosenbluth, and I. Kanter, Fast physical random-number generation based on room-temperature chaotic oscillations in weakly coupled superlattices, *Phys. Rev. Lett.* **111**, 044102 (2013).
 - [9] W. Li, Y. Aviad, I. Reidler, H. Song, Y. Huang, K. Biermann, Y. Zhang, H.T. Grahn, and I. Kanter, Chaos synchronization in networks of semiconductor superlattices, *Europhys. Lett. EPL* **112**, 30007 (2015).
 - [10] Z.Z. Yin, H.L. Song, Y.H. Zhang, M. Ruiz-Garcia, M. Carretero, L.L. Bonilla, K. Biermann, and H.T. Grahn, Noise-enhanced chaos in a weakly coupled GaAs/(Al,Ga)As superlattice,

- Phys. Rev. E* **95**, 012218 (2017).
- [11] T.M. Fromhold, A. Patanè, S. Bujkiewicz, P.B. Wilkinson, D. Fowler, D. Sherwood, S.P. Stapleton, A.A. Krokhin, L.Eaves, M. Henini, N. S. Sankeshwar, and F.W. Sheard, Chaotic electron diffusion through stochastic webs enhances current flow in superlattices, *Nature* **428**, 726 (2004).
 - [12] N. Alexeeva, M.T. Greenaway, A.G. Balanov, O. Makarovskiy, and A. Patanè, High-frequency collective electron dynamics via single-particle complexity, *Phys. Rev. Lett.* **109**, 024102 (2012).
 - [13] S.M. Soskin, I.A. Khovanov, and P.V.E. McClintock, Mechanism of resonant enhancement of electron drift in nanometer semiconductor superlattices subjected to electric and inclined magnetic fields, *Phys. Rev. B* **100**, 235203 (2019).
 - [14] L.L. Bonilla, M. Carretero, and A. Segura, Two dimensional collective electron magneto-transport, oscillations and chaos in a semiconductor superlattice, *Phys. Rev. E* **96**, 062215 (2017).
 - [15] M. Büttiker and H. Thomas, Current instability and domain propagation due to Bragg scattering, *Phys. Rev. Lett.* **38**, 78 (1977).
 - [16] K. Hofbeck, J. Grenzer, E. Schomburg, A.A. Ignatov, K.F. Renk, D.G. Pavel'ev, Yu. Koschurinov, B. Melzer, S. Ivanov, S. Schaposchnikov, and P.S. Kop'ev, High-frequency self-sustained current oscillation in an Esaki-Tsu superlattice monitored via microwave emission, *Phys. Lett. A* **218** 349 (1996).
 - [17] L.L. Bonilla, R. Escobedo, and A. Perales, Generalized drift-diffusion model for miniband superlattices, *Phys. Rev. B* **68**, 241304(R) (2003).
 - [18] M. Alvaro, E. Cebrian, M. Carretero, and L.L. Bonilla, Numerical methods for kinetic equations in semiconductor superlattices, *Comput. Phys. Commun.* **184**, 720 (2013).
 - [19] J.B. Gunn, Instabilities of current and of potential distribution in GaAs and InP, *Procs of Sympos. on Plasma Effects in Solids*, edited by J. Bok, 199–207, Dunod, Paris, France (1965).
 - [20] H. Kroemer, Gunn effect–bulk instabilities, in *Topics in Solid State and Quantum Electronics*, edited by W.D. Hershberger, 20–98, Wiley, New York, USA (1972).
 - [21] L.L. Bonilla and I.R. Cantalapiedra, Universality of the Gunn effect: self-sustained oscillations mediated by solitary waves, *Phys. Rev. E* **56**, 3628 (1997).
 - [22] Y-H. Shiao, Y-C. Cheng and C.-K. Hu, Stochastic postponement of the domain transitions

- and destabilization of current in the Gunn diode, *Phys. Rev. E* **57**, R1227 (1998).
- [23] L.L. Bonilla, R. Escobedo, and F.J. Higuera, Free boundary problems describing two-dimensional pulse recycling and motion in semiconductors, *Phys. Rev. E* **67**, 036202 (2003).
 - [24] S. Le Clainche and J.M. Vega, Higher order dynamic mode decomposition, *SIAM J. Appl. Dyn. Syst.* **16**, 882 (2017).
 - [25] S. Le Clainche and J.M. Vega, Spatio-temporal Koopman decomposition, *J. Nonlin. Sci.* **28**, 1793 (2018).
 - [26] J.M. Vega and S. Le Clainche, Higher Order Dynamic Mode Decomposition and its Applications, *Academic Press* (2020).
 - [27] S. Le Clainche and J.M. Vega, Higher order dynamic mode decomposition to identify and extrapolate flow patterns, *Phys. Fluids* **29**, 084102 (2017).
 - [28] S. Le Clainche, J.M. Perez, J.M. Vega, and J. Soria, Near and far field laminar flow structures in an axisymmetric zero-net-mass-flux jet, *Aerosp. Sci. Technol.* **105**, 105920 (2020).
 - [29] K.H. Park, S.O. Jun, S.M. Baek, M.H. Cho, K.J. Yee, and D.H. Lee, Reduced-order model with an artificial neural network for aerostructural design optimization, *J. Aircraft* **50**, 1106 (2013).
 - [30] C. Gao, W. Zhang, J. Kou, Y. Liu, and Z. Ye, Active control of transonic buffet flow, *J. Fluid Mech.* **824**, 312 (2017).
 - [31] E. Schomburg, T. Blomeier, K. Hofbeck, J. Grenzer, S. Brandl, I. Lingott, A. A. Ignatov, K. F. Renk, D.G. Pavel'ev, Yu. Koschurinov, B. Ya. Melzer, V.M. Ustinov, S.V. Ivanov, A. Zukhov, and P.S. Kop'ev, Current oscillation in superlattices with different miniband widths, *Phys. Rev. B* **58**, 4035 (1998).
 - [32] J.C. Cao and X.L. Lei, Synchronization and chaos in miniband semiconductor superlattices, *Phys. Rev. B* **60**, 1871 (1999).
 - [33] E.M. Mompó, M. Carretero, and L.L. Bonilla, Designing hyperchaos and intermittency in semiconductor superlattices, *Phys. Rev. Lett.* **127**, 096601 (2021).
 - [34] O.M. Bulashenko and L.L. Bonilla, Chaos in resonant-tunneling superlattices, *Phys. Rev. B* **52**, 7849 (1995).
 - [35] K.J. Luo, H.T. Grahn, K.H. Ploog, and L.L. Bonilla, Explosive bifurcation to chaos in weakly-coupled semiconductor superlattices, *Phys. Rev. Lett.* **81**, 1290 (1998).
 - [36] O.M. Bulashenko, K.J. Luo, H.T. Grahn, K.H. Ploog, and L.L. Bonilla, Multifractal dimension

- of chaotic attractors in a driven semiconductor superlattice, *Phys. Rev. B* **60**, 5694 (1999).
- [37] A. Carpio, P.J. Hernando, and M. Kindelan, Numerical study of hyperbolic equations with integral constraints arising in semiconductor theory, *SIAM J. Numer. Anal.* **39**, 168 (2001).
 - [38] P.J. Schmid and J.L. Sesterhenn, Dynamic Mode Decomposition of numerical and experimental data, *Amer. Phys. Soc.*, 61st APS Meeting, 23–25 November, San Antonio, CA, USA (2008).
 - [39] P.J. Schmid, Dynamic mode decomposition of numerical and experimental data, *J. Fluid Mech.* **656**, 5 (2010).
 - [40] T.G. Kolda and B.W. Bader, Tensor decompositions and applications, *SIAM Review* **51**, 455 (2009).
 - [41] L.S. Lorente, J.M. Vega, and A. Velazquez, Generation of aerodynamic databases using high-order singular value decomposition, *J. Aircraft* **45**, 1779 (2008).
 - [42] G.H. Golub and G.T. van Loan, Matrix Computations, *John Hopkins Univ. Press* (1996).
 - [43] T. Bui-Thanh, Proper Orthogonal Decomposition, Extensions and their Applications in Steady Aerodynamics, *Master Thesis: Singapore-MIT Alliance*, 2003.
 - [44] T. Bui-Thanh, M. Damodaran, and K. Willcox, Aerodynamic data reconstruction and inverse design using Proper Orthogonal Decomposition, *AIAA Journal* **42** 1505 (2004).
 - [45] S. Le Clainche and J.M. Vega, Analyzing nonlinear dynamics via data-driven dynamic mode decomposition-like methods, *Complexity* **2018**, 6920783 (2018).
 - [46] S. Le Clainche, J.M. Vega, and J. Soria, Higher order dynamic mode decomposition for noisy experimental data: flow structures on a Zero-Net-Mass-Flux Jet, *Exp. Therm. and Fluid Sci.* **88**, 336 (2017).
 - [47] S. Le Clainche, F. Sastre, J.M. Vega, and A. Velazquez, Higher order dynamic mode decomposition applied to study flow structures in noisy PIV experimental data, *Proc. 47th AIAA Fluid Dynamics Conference*, AIAA paper 2017-3304 (2017).
 - [48] S. Le Clainche, L.S. Lorente, and J.M. Vega, Wind predictions upstream wind turbines from a LiDAR database, *Energies* **11**, 543 (2018).
 - [49] S. Le Clainche, X. Mao, and J.M. Vega, New method to capture traveling waves in flow passing a wind turbine, *Wind Energy* **22**, 922 (2018).
 - [50] S. Le Clainche, R. Moreno-Ramos, P. Taylor, and J.M. Vega, New robust method to study flight flutter testing, *J. Aircraft* **56**, 336 (2019).

- [51] C. Mendez, S. Le Clainche, R. Moreno-Ramos, and J.M. Vega, A new automatic, very efficient method for the analysis of flight flutter testing data, *Aerosp. Sci. Technol.* **114**, 106749 (2021).
- [52] V. Beltran, C. Mendez, S. Le Clainche, and J.M. Vega, Wake interactions in multibody configurations with different shape, *Aerosp. Sci. Technol.* **95**, 105428 (2019).
- [53] J. Sánchez, M. Net, and J.M. Vega, Analyzing thermal convection in a two-dimensional circular annulus via spatio-temporal Koopman decomposition, *Physica D* **402**, 132257 (2020).
- [54] W.H. Press, S.A. Teukolsky, W.T. Vetterling, and B.P. Flannery, Numerical Recipes in C: The Art of Scientific Computing, *Cambridge Univ. Press* (1988).
- [55] J. Laskar, Frequency analysis of a dynamical system, *Celestial Mech. Dyn. Astron.* **56**, 191 (1993).
- [56] J. Laskar, Frequency analysis for multi-dimensional systems, *Physica D* **67**, 257 (1993).
- [57] K.K. Chen, J.H. Tu, and C.W. Rowley, Variants of dynamic mode decomposition: boundary condition, Koopman and Fourier analyses, *J. Nonlinear Sci.* **22** 8871 (2012).
- [58] <https://github.com/LeClaincheVega/HODMD>
- [59] A. Meseguer, Fundamentals of Numerical Mathematics for Physicists and Engineers, *Wiley* (2020).